

THESIS FOR THE DEGREE OF DOCTOR OF PHILOSOPHY

A computational study of interface structures and  
energetics in cemented carbides and steels

SVEN JOHANSSON

Department of Applied Physics  
CHALMERS UNIVERSITY OF TECHNOLOGY  
Göteborg, Sweden 2010

A computational study of interface structures and energetics in cemented carbides  
and steels

Sven Johansson

ISBN 978-91-7385-387-3

© Sven Johansson, 2010.

Doktorsavhandlingar vid Chalmers tekniska högskola

Ny serie nr. 3068

ISSN 0346-718X

Department of Applied Physics

Chalmers University of Technology

SE-412 96 Göteborg, Sweden

Telephone +46-(0)31-772 1000

Chalmers reproservice

Göteborg, Sweden 2010

A computational study of interface structures and energetics in cemented carbides and steels

Sven Johansson

Department of Applied Physics

Chalmers University of Technology

## ABSTRACT

Cemented carbides are hard composite materials of great industrial importance. Because of their combination of hardness and toughness, they are used e. g. for cutting, drilling, turning and milling. The material is produced by means of powder metallurgy, where powders of carbide and metal are sintered together into a hard and dense material. To retain a fine WC-Co microstructure, additions of VC, Cr<sub>3</sub>C<sub>2</sub>, TiC etc. are often made to inhibit WC grain growth.

In this thesis, a computational study of interface structures and energetics in WC-Co cemented carbides is presented. The investigation is performed in the density functional theory framework with a plane-wave pseudopotential method. To make predictions of interface energies, coherent atomic interface configurations are used.

We have calculated the stability of thin layers of cubic TiC, VC, CrC, NbC, MoC, HfC and TaC in the interface between WC and Co. Due to a lowering of the WC/Co interface energy, we predict that thin VC films of two atomic layers are stable at the basal WC/Co interfaces at high temperature sintering conditions under which grain growth occurs. The predicted atomic structure is in agreement with available high-resolution electron microscopy images. A comparison between the stability of various carbide films in both basal and prismatic WC/Co interfaces provides a consistent explanation for the experimentally known effectiveness of VC as grain growth inhibitor.

Furthermore, we have extended our modeling of interfaces to include the effect of misfit in semicoherent interfaces. Information of interface energetics from atomistic simulation is coupled to a continuum model of elasticity in the Peierls-Nabarro scheme to account for misfit dislocations. The method is applied to the low misfit Fe/VN interface in steels, and we find that its interface energy is dominated by elastic energy.

**Keywords:** cemented carbides, WC-Co, interfaces, sintering, microstructure, density functional theory, steels



## LIST OF PUBLICATIONS

This thesis consists of an introductory text and the following papers:

- I Theory of ultrathin films at metal-ceramic interfaces**  
S. A. E. Johansson and G. Wahnström  
Accepted for publication in *Phil. Mag. Lett.*
- II A computational study of cubic carbide films in WC/Co interfaces**  
S. A. E. Johansson and G. Wahnström  
In manuscript.
- III Energetics and structure of interfaces in WC-Co alloys from first-principles calculations**  
M. Slabanja, S. A. E. Johansson and G. Wahnström  
In: L. S. Sigl, P. Rödhammer, H. Wildner (Eds.), *Proceedings of the 17th International Plansee Seminar*, vol. 2, Plansee Group, Reutte, Tyrol, Austria, 2009, p. HM2.
- IV Transition metal solubilities in WC in cemented carbide materials**  
J. Weidow, S. A. E. Johansson, H.-O. Andrén and G. Wahnström  
Submitted to *J. Am. Ceram. Soc.*
- V Interface energy of semicoherent metal-ceramic interfaces**  
S. A. E. Johansson, M. Christensen and G. Wahnström  
*Phys. Rev. Lett.* **95**, 226108 (2005).
- VI Theoretical investigation of moderate misfit and interface energetics in the Fe/VN system**  
D. H. R. Fors, S. A. E. Johansson, M. Petisme and G. Wahnström  
Submitted to *Phys. Rev. B*.

Scientific papers not included in this thesis:

**VII Effect of Co magnetism on the solid state sintering of WC-Co alloys**

V. Bounhoure, S. A. E. Johansson, S. Lay, J. M. Missiaen and G. Wahnström  
In manuscript.

My contributions to the appended papers are:

I-II. I did all DFT calculations, modeling and wrote the papers.

III. I did a minor part of the DFT calculations. The paper was written jointly.

IV. I did all DFT calculations and modeling. The paper was written jointly.

V. I setup the model, did the atomistic and elastic modeling as well as some of the DFT calculations. The paper was written jointly.

VI. I did the analytical parts of the elastic modeling.

# Contents

<b>1</b>	<b>Introduction</b>	<b>1</b>
<b>2</b>	<b>Materials</b>	<b>5</b>
2.1	Cemented carbides . . . . .	5
2.1.1	Manufacturing and sintering . . . . .	6
2.1.2	The W-C-Co phase diagram and carbon balance . . . . .	8
2.1.3	Carbide and binder . . . . .	9
2.1.4	Microstructure . . . . .	11
2.1.5	Additions . . . . .	15
2.2	Steels . . . . .	20
<b>3</b>	<b>Computational methods</b>	<b>23</b>
3.1	First-principles calculations . . . . .	24
3.1.1	Density functional theory . . . . .	25
3.2	Semiempirical methods . . . . .	29
3.3	Elasticity theory . . . . .	31
<b>4</b>	<b>Thermodynamics and modeling of interfaces</b>	<b>35</b>
4.1	Thermodynamics . . . . .	36
4.1.1	Thermodynamics of interfaces . . . . .	36
4.1.2	Connecting DFT and thermodynamics . . . . .	38
4.1.3	Solubility . . . . .	42
4.2	Interface modeling . . . . .	44
<b>5</b>	<b>Conclusions</b>	<b>51</b>
5.1	Summary . . . . .	51
5.2	Outlook . . . . .	52
	<b>Acknowledgments</b>	<b>55</b>
	<b>Bibliography</b>	<b>57</b>

**Papers**

**69**

## Introduction

The 20th century saw a revolutionary increase of industrial productivity. As an example, in the manufacturing industry the development of cutting tools for steel machining has had huge impact; cutting speeds have increased at least hundred-fold since the late 1800s' use of plain carbon steels [1], and consequently, the time needed for machining a given volume steel has decreased to a hundredth or thousandth. Particularly in the decades following the commercial introduction in the 1920s, the increasing cutting efficiency was achieved by the development and improvements of the material known as cemented carbide. Because of their successful combination of hardness and toughness, cemented carbides are used in diverse applications including rock drilling, machining of wood, plastics and composites, wear parts and ammunition. Measured by total use, metal cutting is the most important application [2].

The term 'cemented carbides' refers to the structure of the material, in which hard carbide grains are cemented in a ductile iron group metal binder (see Fig. 2.6). Produced by powder metallurgical methods, the desired microstructures are obtained by sintering a mixture of carbide and metal powders above the melting temperature of the metal. The first grades of cemented carbide were based on plain WC-Co, which still retains industrial importance especially in applications demanding toughness. Early developments included the addition of cubic carbides (TiC, NbC, TaC, etc.) to improve steel-cutting properties. Cemented carbides are sometimes synonymously called hardmetals, although the latter term can take a broader meaning and also include nitride- and carbonitride-based materials (e. g. Ti(C,N)-Ni) often referred to as 'cermets'. In this thesis, only carbides with Co binder are considered.

Over the years, numerous experimental investigations have been carried out on the cemented carbides systems focusing on aspects such as sintering behavior, microstructure, mechanical behavior and wear properties [3]. Thus, on a macroscopic level, the system is generally well studied and characterized, and a large part of cemented carbide development has been purely empirically based. To gain a deeper

understanding of the material, its microstructure and constituents, it is necessary to study the microscopic and atomic level. The advancement of experimental instrumentation in the last decades clearly has clearly facilitated atomic-scale studies. Atom-probe tomography allows a 3D atomic reconstruction with a resolution below 1 nm with chemical identification of the atoms. For more detailed studies of atomic structure, high-resolution transmission electron microscopy can be used to identify lattice structures in bulk and interfaces. In the statistical sense, electron backscatter diffraction in the scanning electron microscope provide information on grain shapes, sizes and interfacial orientation relationships.

As for any multiphase polycrystalline material (and apparent when studying Figs. 2.6 and 2.7), the cemented carbide owes its properties both to the bulk phases and their corresponding interfaces. The energetics of the interfaces directly influence the subprocesses occurring in the sintering process thus providing the driving force behind the metal wetting of the carbide, densification and grain growth. Of course, the adhesion properties of intraphase and grain boundaries are also important for mechanical properties.

Theoretically, the occurring bulk phases, their structure and composition, are well described by models of phase equilibria and transformations within the field of computational thermodynamics [4]. Both the thermodynamic method and the description of the W-C-Co system with additions of various carbide formers has reached a high level of maturity. However, these models do not incorporate the effect of interfaces. Despite the availability of advanced experimental techniques, predictive modeling of interface energetics and structures based only on experimental data is likely not feasible – at least not without lengthy experiment series and analyses. Interface energies are notoriously difficult to measure, and the available estimations for the carbide-cobalt systems mostly stem from wetting experiments.

Fortunately, today's computational power and efficient theoretical tools as density functional theory allow the calculation of materials properties directly from first-principles. Thus, theoretical calculations can provide otherwise unattainable quantitative data of bulk and interfacial energetics. Of course, an exclusively theoretical approach on its own would be of little value in materials science. Firstly, experimental information from the experimental techniques mentioned above provide valuable input for atomistic models in theoretical calculations. Secondly, apart from acting as mere validation, the comparison between theoretical predictions and experimental results is probably the occasion where the best insight is attained.

This thesis is devoted mainly to first-principles density functional theory (DFT) calculations of interfaces. The first four appended papers concern the W-C-Co system. In Papers I and II, the formation of cubic carbide films in WC/Co interfaces is studied. Paper III treats the energetics of WC/Co interfaces in plain W-C-Co. In Paper IV, the solubility of some transition metals in WC is studied.

Papers V and VI treat a disparate materials class – steels – but share the computational methods of the other papers. In Papers V and VI, an elastic correction to semicoherent interface energies is introduced, which is of general applicability. The papers are included as they represent a methodological extension to the modeling of

---

interfaces done by Dudy [5] and Christensen [6].

The introductory text is organized accordingly: Chapter 2 introduces the material classes under study and provide background information on the issues studied in the papers. In Chapter 3, the computational methods used are presented. Chapter 4 describes the atomistic modeling used in the papers. The main results of the thesis work are summarized in Chapter 5.



# Materials

This chapter provides a brief background on the two materials under study in this thesis: cemented carbides (Paper I-IV) and steels (Paper V-VI) with a main focus on the former.

## 2.1 Cemented carbides

The history of cemented carbides began in the end of the 19th century, when the French scientist Henri Moissan synthesized and characterized hard compounds formed by transition metals in combination with boron, carbon, and nitrogen. Around 1920, the German scientists in the Osram Studiengesellschaft were given the task of replacing diamond in the drawing dies used in tungsten filament production. Earlier attempts by German scientists to utilize Moissan's findings had given a coarse-grained material that was hard but also brittle. Having long experience of tungsten metallurgy from its applications in the electrical industry, the Osram team found a way of synthesizing tungsten and carbide powder into a fine-grained tungsten carbide. However, it was not until the addition of a metal from the iron group that the group made its important break-through. Eventually, Co turned out to be the best additive. Accounts of the history of cemented carbides can be found in Refs. [1, 7].

From the first attempts of the Osram team, the properties of cemented carbides developed steadily in subsequent decades by the introduction of other carbide formers such as Ti, Ta, and Nb, and grain growth inhibitors such as Cr and V. A major leap in the development of cemented carbides was taken with the introduction of hard and wear-resistant coatings in the late 1960s. Chemical and, more recently, physical vapour deposition is used to apply combinations of TiC, TiN, Al<sub>2</sub>O<sub>3</sub>, etc. layers forming a coating with a thickness of roughly 10 μm, which can prolong the lifetime of a tool by a factor 10 [8]. Today, potential benefits of composition changes of the cemented carbide are probably largely exhausted, and the past two decades considerable effort has been devoted to producing cemented carbides of yet finer

grades [9, 10]. Current development of cemented carbides is focused on optimizing the bulk material in combination with the coating and geometry of the carbide substrate [11].

### 2.1.1 Manufacturing and sintering

Production of cemented carbides is done by means of powder metallurgy, where powders of carbide and metal are mixed and heated to form a dense material. The process from raw material to finished product includes several steps which all to varying degree affect the microstructure of the final material [12, 13]. Here, a brief overview of the manufacturing process is given. More details can be found in the literature covering the subject (see e. g. [14, 15, 3, 2]).

WC powder production starts with hydrogen reduction of  $\text{WO}_3$  to form W powder, which upon carburization transforms into WC. Direct carburization of  $\text{WO}_3$  is also possible. Typical grain sizes of conventionally produced WC powder range from 0.15 to  $12\mu\text{m}$  [2]. Also Co is supplied as a powder obtained conventionally from reduction of cobalt oxides.

The first step in consolidating the cemented carbide is to mill the powders to obtain a homogeneous mixture and to decrease the carbide grain size. Both alcohol, used as a milling liquid, and a wax providing firmness to the unsintered product, are added during this stage. After drying the milled powders from alcohol, the agglomerated powder (the green body) is pressed, usually uniaxially, to the desired shape. The shape will be approximately retained throughout the sintering, whereas the linear shrinkage will be 17 – 25 % [2].

The object of the sintering is to strengthen the material by eliminating pores and creating strong intergrain adhesion. This is accomplished by heating the green body in a furnace of well-controlled temperature and atmosphere. The heat treatment is performed in several steps and a typical sintering cycle is depicted in Figure 2.1. First, the temperature is ramped up to around  $400^\circ\text{C}$  eliminating the wax added before milling. From this level, the temperature is gradually increased to the final sintering temperature of around  $1400^\circ\text{C}$  with some holds along the way to permit outgassing of carbon oxides originating from the reduction of surface oxides on the WC powder surfaces. The melting of the binder at around  $1300^\circ\text{C}$  divides the solid state and liquid phase sintering.

Solid state and liquid phase sintering share many similarities. In both, the driving force behind the sintering process is the reduction of surface and interface energies which induces a mass transport leading to densification and grain growth. It has been established that a significant part of sintering as measured by the densification occurs in the solid state [16]. In fact, for fine-grained materials with grain sizes in the micrometer and submicrometer scale, the major part of sintering occurs already in the solid state [17, 18, 10].

The sintering starts at around  $800^\circ\text{C}$  or even lower for nano-sized grains (of diameters  $\leq 500\text{nm}$ ) [19]. This is also the temperature at which W atoms from WC grains start to dissolve into the binder [20]. At the onset temperature, surface oxides

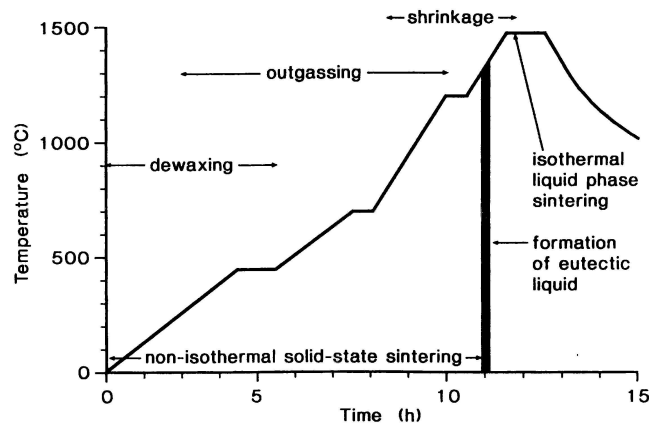


**Figure 2.1:** A typical sintering cycle of cemented carbides from [2].

have been reduced which allows Co to spread on WC surfaces. The spreading takes place by diffusion and viscous flow driven by capillary forces, and induces a WC particle rearrangement. It has been speculated that Co spreading is preceded by a fast spreading of a sub-monolayer film of Co, which rapidly diffuses on WC surfaces as surface oxides are reduced and on top of which the Co front may flow easily [21]. After initial spreading, the process continues with a filling of small pores and formation of agglomerates of WC particles bound by Co [22]. Between 1000 and 1200°C the pore structure between agglomerates collapses [19]. The decrease of void space is necessarily accompanied by grain shape accommodation and grain growth. These processes occur by Ostwald ripening, where smaller grains due to their large relative surface area dissolve and the W and C atoms reprecipitate in equal amounts on larger WC grains. This leads to a change in morphology, as reprecipitation preferably occurs on low-energetic interfaces making the grains more faceted. At 1200°C, the WC grains have largely changed shape into their characteristic triangular platelet shape [19].

It should be pointed out that the description and temperatures in the preceding paragraph applies to nano-sized grains. For coarser materials, the densification processes are postponed to higher temperatures and larger part of densification occurs at isothermal holding at liquid phase sintering. For micrometer-sized grains, the faceting of WC is not evident until 1300°C [19], which is close to or over the melting temperature of the binder. In the liquid phase, solubility and diffusion of W and C atoms in the binder phase is larger and thus the densification is more rapid. Also the most fine-grained materials need to be heated into the liquid phase to achieve complete densification. Whereas for fine-grained materials densification and grain growth occur more or less concurrently, the liquid phase sintering of coarser materials can generally be divided into the three distinguishable stages of rearrangement, solution/reprecipitation and grain coalescence [23].

As the furnace cools from liquid phase sintering temperatures, further grain growth occurs as a result of the decreasing W and C solubilities in the binder. W diffusion is estimated to freeze at temperatures somewhere between 800 and 900°C,

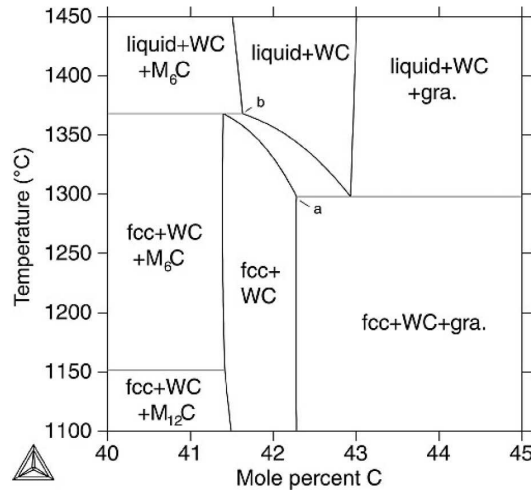


**Figure 2.2:** A section of the W-C-Co phase diagram at 15.5 at.% Co from [24]. To avoid possible formation of  $M_6C$  ( $\eta$ -phase) or graphite upon cooling, the carbon content must be kept between points 'a' and 'b'. Melting of the binder starts at 1298 °C (1368 °C) for C-rich (-poor) WC-Co.

where the exact value depends on the local geometry of the interphase boundary [20].

The heating and sintering temperature and time are important process parameters. On one hand, full densification and uniformity of the material are desired, but on the other hand, grain coarsening deteriorates mechanical properties. The optimal sintering route must be determined from the composition and grain size distribution at hand.

### 2.1.2 The W-C-Co phase diagram and carbon balance

The WC and binder phases are often denoted  $\alpha$  and  $\beta$ , respectively. The carbon content of the material is a critical process parameter and needs to be meticulously tuned to reach the desired window of the phase diagram as depicted in Figure 2.2. Lack of carbon induces the formation of  $(Co,W)_6C$  ( $\eta$ -phase), whereas a surplus yields graphite precipitates. Both act strongly deteriorating on materials properties and care must be taken to avoid their formation. This is more difficult in grades of low Co content, as the two-phase ( $\alpha + \beta$ ) field narrows for lower binder fraction (see Figure 2.3). Guidance to a correct initial composition is accurately provided by mathematical models of phase equilibria and thermodynamical databases [25]. However, the carbon content is also affected by the atmosphere of the furnace and, more importantly, carbon is consumed in the reduction of surface oxides during the heating. Therefore, extra carbon is usually added to the powder mix before sintering. The amount needed depends on e. g. WC grain size and milling time, and maintaining the right carbon balance is a matter of experience.

Rather than the gross carbon content, it is the carbon activity  $a_C$  that determines the microstructural development during sintering. In Figure 2.4, the phase diagram

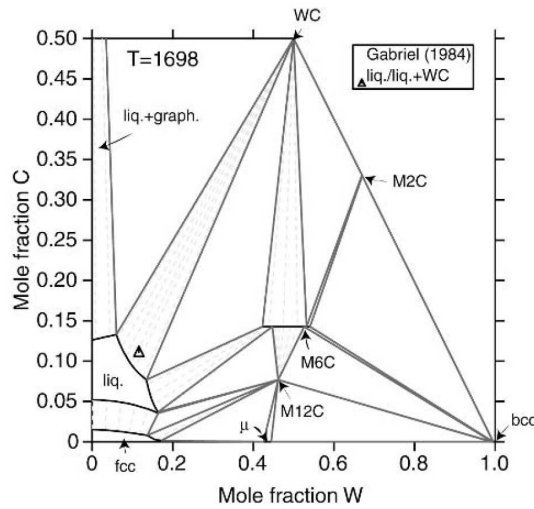


**Figure 2.3:** The W-C-Co phase diagram at 1425 °C from [25]. The temperature lies in the range of common liquid phase sintering temperatures used in hard metal production. The two-phase (WC+Co) field narrows as the Co content decreases. Solubilities in the liquid of 6 at.% W and 13 at.% C (14 at.% W and 8 at.% C) at the C-rich (-poor) limit of the WC+Co field can be read off the diagram.

of the W-C-Co system is given as function of carbon activity. From a computational point of view, a definite value of the carbon chemical potential  $\mu_C$  is needed to define absolute values of e. g. interface energies.  $a_C$  and  $\mu_C$  are simply related (see e. g. [4]). In the appended papers, we let  $\mu_C$  vary between limits corresponding to formation of graphite and  $\eta$ -phase, respectively. This interval is slightly less than 0.2 eV wide and has a weak temperature dependence (from the models in Ref. [25]). In the three-phase fields (WC+Co+ $\eta$  and WC+Co+graphite),  $\mu_C$  is constant as function of carbon content.

### 2.1.3 Carbide and binder

WC has a hexagonal structure of space group  $P\bar{6}m2$  with lattice parameters  $a = 2.906 \text{ \AA}$  and  $c = 2.837 \text{ \AA}$  [2]. Two sets of planes are of special interest. These are the basal planes  $\{0001\}$  and the prismatic planes  $\{10\bar{1}0\}$ . Due to the geometry, the prismatic surfaces exist in two non-equivalent types (denoted I and II) depending on the interplanar distance between the first and second layer of atoms. A drawing of the lattice structure with the important surfaces is provided in Figure 2.5. During sintering, the WC grains grow preferably on the prismatic and basal surfaces [14], which results in strong faceting and a tendency for the grains to acquire a truncated triangle shape. An example of the microstructure and a typical WC grain shape is given in Figure 2.6. The equilibrium WC grain shape in Co, which is determined by the WC/Co interface energetics, has been investigated experimentally and from first-principles [26]. The truncated triangular shape arises from an energetic difference between prismatic WC/Co interfaces of type I and II, and both experimental and theoretical results show that the grain shape becomes less truncated for increasing

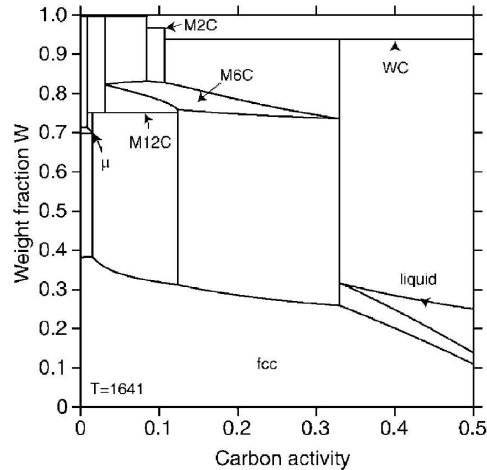


**Figure 2.4:** The W-C-Co phase diagram at 1641 K from [25]. At this temperature,  $\eta$ -phase forms at a carbon activity of around 0.33, which corresponds to a carbon potential of  $-0.16\text{ eV}$  with respect to graphite. A four-phase equilibrium exists (WC+fcc Co+liquid Co+ $M_6C$ ) corresponding to the point marked ‘b’ in Figure 2.2.

carbon activity [26].

In the W-C phase diagram, WC exists in a very small range of homogeneity with a carbon content corresponding to perfect stoichiometry (50 at.% W and 50 at.% C) [14] meaning that, in practice, W and C vacancies can be assumed not to occur. Except for Mo [27], the solubilities of other transition metals in WC have also been assumed insignificant ([14] and references in [3]) and have therefore, as far as we know, not yet been considered in thermodynamic modeling of the WC phase. However, recent experiments have indicated a sizable Cr solubility in WC [28, 29]. In Paper IV, we investigate the solubility of several group IV-B to VI-B transition metals in WC.

Cobalt is the most commonly used binder in cemented carbides [2]. Its complete wetting of WC combined with the mechanical properties of the sintered material – in particular the toughness – makes it the most suitable binder for a broad spectrum of applications. Iron and nickel are other possible binder metals in cemented tungsten carbides, though the latter has larger use as binder alone or in conjunction with Co in cermet grades based on Ti(C,N) [30].

The stable structure of Co is hexagonal close-packed (hcp) up to  $422^\circ\text{C}$ , where Co transforms into the face-centered cubic (fcc) structure [31]. Pure Co melts at  $1495^\circ\text{C}$  [31], but the melting temperature is lowered by dissolved W and C (see Figure 2.2). The solubility of WC in Co is appreciable, and considerably higher than the WC solubility in Ni or Fe [14]. The respective W and C solubilities are determined by the carbon activity and temperature. Some typical values for liquid phase sintering temperatures are given in the caption of Figure 2.3. After cooling, a large fraction of the dissolved W atoms is retained in the binder due to the slow diffusion. W in solid solution has positive effects, as it strengthens the material and makes it more resistant against plastic deformation [2].

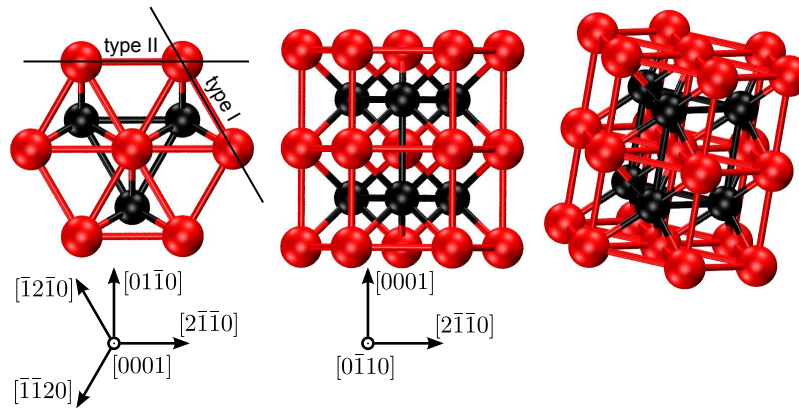


**Figure 2.5:** The lattice structure of hexagonal WC with some important directions. W atoms are depicted brighter and larger than C atoms. A possible choice of lattice vectors is  $\vec{a}_1 = a\hat{x}$ ,  $\vec{a}_2 = -a/2\hat{x} + \sqrt{3}/2\hat{y}$  and  $\vec{c} = c\hat{z}$ . Left: The structure is viewed towards the basal (0001) surface. Two non-equivalent types of W-terminated prismatic surfaces are outlined. Interplanar distances between the first and second atomic layer as well as relative atomic positions differ between the surfaces of type I and II. Middle: The structure is viewed towards the prismatic (0110) surface.

At room temperatures, the metastable fcc Co phase usually dominates the binder in a sintered WC-Co cemented carbide (see, e. g. Ref. [32]). The high temperature fcc phase is suggested to be stabilized by dissolved W and C which lower the starting temperature of the martensitic transformation of the fcc phase into hcp [33]. The transformation is achieved by the motion of partial dislocations, but dissolved W and C atoms as well as WC grains hinder this motion. A notable feature of the cubic binder in liquid phase sintered WC-Co is its large grain size which can be in the millimeter range [14]. Thus, Co/Co grain boundaries are rarely seen in the sintered material. The large Co grain sizes have been explained by the scarcity of nucleation sites available when the melt solidifies, allowing a single grain to grow large distances before impinging another grain.

Although ferromagnetic at low temperatures, Co is paramagnetic above its Curie temperature of 1123 °C [31]. The Curie temperature is lowered by solutes, and for Co in C-rich (C-poor) WC-Co it is around 1051 °C (933 °C) (from the model of [34]).

#### 2.1.4 Microstructure

When studying a magnified image as Figure 2.6 of a sintered cemented carbide, it becomes apparent that the microstructure is important for mechanical properties of the sintered material. In this section, important experimental observations of the microstructure in the WC-Co system will be presented with an emphasis on the atomic structure of interfaces and grain boundaries.

From high-resolution transmission electron microscopy (TEM) images, it can be deduced that WC/Co interfaces are, at least locally, planar and sharp [35]. In

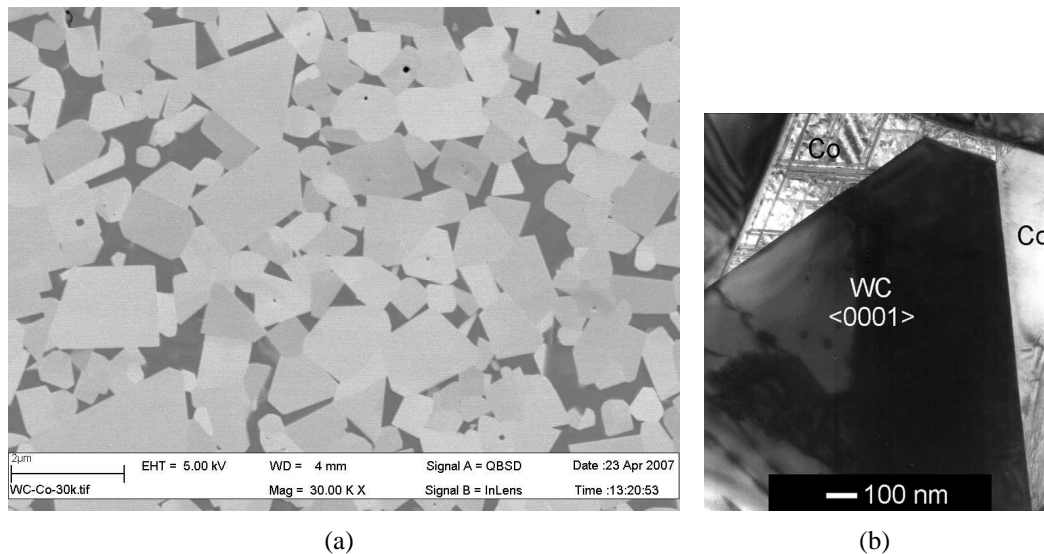


**Figure 2.6:** (a) A SEM image of the microstructure of WC-Co without dopants. The bright parts correspond to the carbide grains and the binder appears dark. The material in the image has the composition 9.89 wt% Co, 5.41 wt% C and 84.70 wt% W. The measured WC average grain size is  $0.708\ \mu\text{m}$ . Courtesy of J. Weidow. (b) A TEM image of a WC grain in Co with a typical truncated triangular shape. Courtesy of S. Lay.

W-rich alloys, WC/Co interfaces are sometimes slightly rounded and contain steps with side lengths in the order of 10 nm, whereas in C-rich alloys the interfaces are almost perfectly sharp and faceted after liquid phase sintering [36]. WC/WC grain boundaries can be curved at lower temperatures ( $1200^\circ\text{C}$ ), but tend to straighten at higher temperatures and longer sintering times [36, 37].

Characterization of grain boundaries is often done in terms of the misorientation and coincident site lattice (CSL) of the adjoining crystals (see, e. g. [38] for details on these concepts). Since the ratio  $c/a = 0.976$  for WC is close to 1, it is possible for WC to form several low  $\Sigma$  boundaries in the  $c/a = 1$  approximation [39]. Notably, a  $90^\circ$  rotation around a common  $[10\bar{1}0]$  axis gives rise to a  $\Sigma 2$  boundary [39]. A sketch of two special types (twist and tilt) of  $\Sigma 2$  boundaries of WC is given in Figure 2.8.

The determination of orientational relationships in grain boundaries and interfaces has been immensely simplified with the introduction of the electron backscatter diffraction technique (EBSD) in the scanning electron microscope (SEM) [40]. Automated measurements of misorientation axes and angles in grain boundaries in large enough numbers to allow for statistical analysis are now possible, which would have been unfeasible with the more labor-demanding TEM. EBSD has thus become an important tool for quantitative characterization of microstructure.

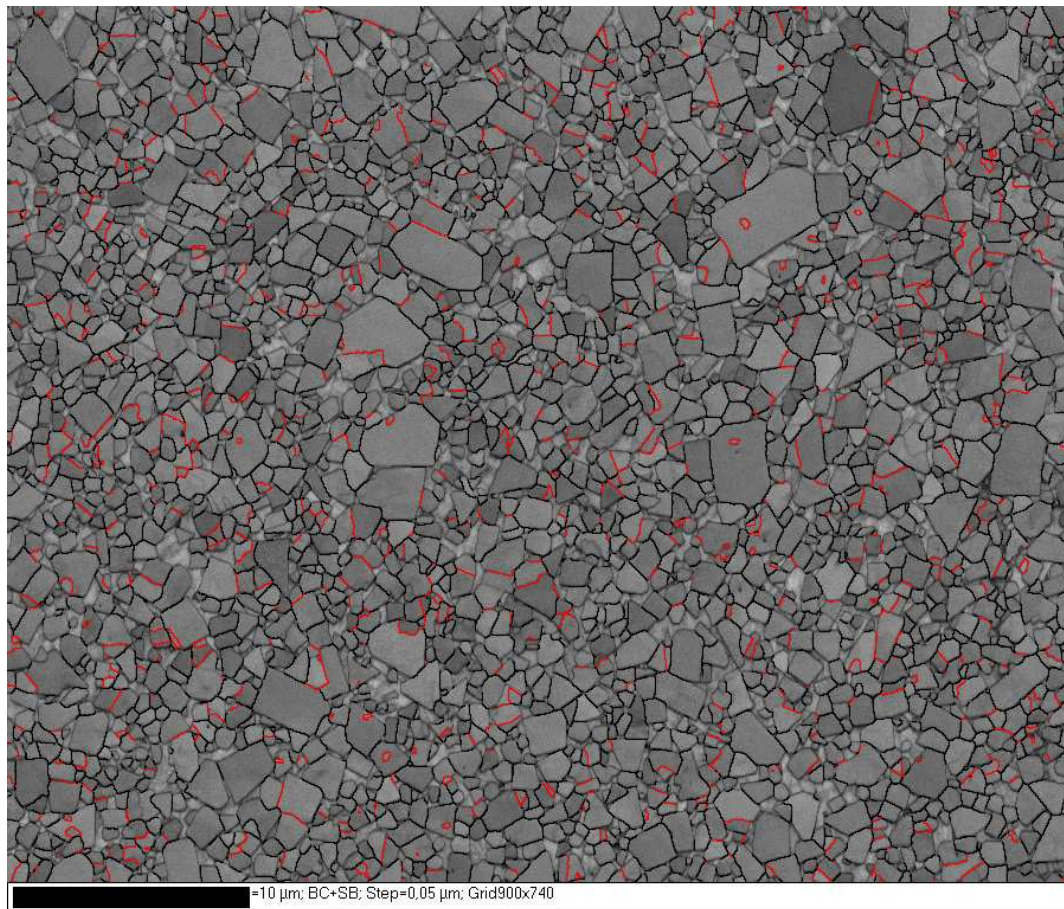
An image created from EBSD data of a WC-Co microstructure is given in Figure 2.7(a) with the associated distribution of WC/WC misorientation angles in Figure 2.7(b). Apart from the large low-angle contribution, an outstanding feature of the misorientation distribution is the distinct peak at  $90^\circ$ , which also exists in other published distributions [41, 42, 43, 44]. In Ref. [41], the  $90^\circ$  peak is shown to be associated with  $\langle 10\bar{1}0 \rangle$  rotation axes, and the peak therefore represents  $\Sigma 2$  boundaries.

The  $\Sigma$ -value and misorientation of a grain boundary does not provide information on the interface planes. However, with data from EBSD the distribution of interface planes can be determined in a statistical sense [41]. In Ref. [44] it is concluded that most  $\Sigma 2$  boundaries have  $\{10\bar{1}0\}$  habit planes and thus are pure twist boundaries.

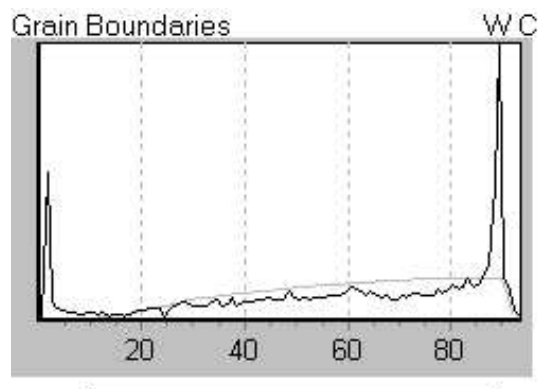
It has been shown that the fraction of  $\Sigma 2$  boundaries of all WC/WC grain boundaries decreases as sintering proceeds [43, 37]. The same observation is made in doped WC-Co, in which small grain size correlates with large fraction of  $\Sigma 2$  [32, 45]. It can therefore be argued that the  $\Sigma 2$  boundaries stem from grain boundaries present already in the powder [42], which is supported by TEM investigations of WC clusters in the powder [46]. Thus, although the  $\Sigma 2$  twist boundary has a remarkably low grain boundary energy [47], it does not seem to form preferentially during sintering, and the fraction of  $\Sigma 2$  decreases as small grains dissolve and new grain boundaries form. The origin of the  $\Sigma 2$  boundaries is possibly related to preferential directions of carburization of W or  $W_2C$ , but available literature is scarce on the subject.

In general, WC/WC grain boundaries in the sintered material contain segregated Co. Experimental estimations of the amount of Co in grain boundaries do, however, vary and a long-standing question has been whether WC grains form a continuous skeleton or if the binder phase infiltrates all grain boundaries to form a continuous skin over the WC grains. The latter model is supported by Sharma *et al.*, who reported the presence of Co films with a thickness of several monolayers between WC grains from TEM and x-ray spectroscopy measurements [48]. Later atom-probe and analytic TEM measurements by Henjered *et al.* suggest that Co segregates in sub-monolayer proportions to grain boundaries supportive of a WC skeleton model [49]. However, it has also been found that some special grain boundaries are free from segregated Co. By energy dispersive x-ray analysis in the TEM, Vicens *et al.* noticed that WC grain boundaries with dense boundary planes (basal or prismatic), e. g. a  $\Sigma 2$  twist boundary, contain no Co, but that, in general, the Co segregation amount does not correlate with the  $\Sigma$  value of the boundary [50]. First-principles calculations of the  $\Sigma 2$  tilt boundary suggest that segregation of Co in sub-monolayer proportions lowers its grain boundary energy [51]. If the tilt boundary can be seen as representative of a general WC/WC grain boundary, these results would support the conclusions of Ref. [49].

Upon solidification of the binder phase after liquid phase sintering, Co grains grow without any preference to orientations of the embedded WC grains. Thus, unlike WC/WC boundaries, WC/Co interfaces do not generally show any orientation structure, although it is clear that the WC boundary planes are predominantly basal  $\{0001\}$  and prismatic  $\{10\bar{1}0\}$  (as quantitatively shown in Ref. [44]). However, in small Co pools between WC grains, Co orientations different from the surrounding Co matrix have been observed in the TEM [52]. In the observed Co pools, dense (111) or (001) planes align with the basal WC surface. Interfaces bounded by WC(0001) and Co(111) surfaces have also been reported for Co inclusions in WC grains [53, 54]. In solid state sintered WC-Co, these special orientations between WC and Co are frequently found, and for W-rich WC-Co a majority of interfaces involving the WC basal surfaces have either a WC(0001)  $\parallel$  Co(111) or



(a)



(b)

**Figure 2.7:** (a) An image created from EBSD data of a WC-Co specimen. Boundaries with a misorientation within approximately  $\pm 10^\circ$  from  $90^\circ$  are red. This misorientation makes them possible  $\Sigma 2$  boundaries. Remaining grain boundaries are black. (b) The misorientation angle distribution for the specimen in (a). The frequency of a random distribution is given in light gray. A peak at  $90^\circ$  is visible. Courtesy of J. Weidow.

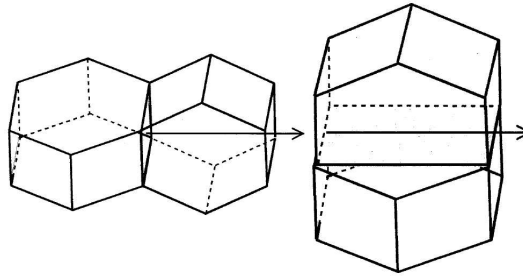


**Figure 2.8:** Simple sketches of the (left) pure twist and (right) pure tilt  $\Sigma 2$  boundaries. The common rotation axis is the prismatic  $[10\bar{1}0]$  axis. Denoting the adjoining crystals 1 and 2, the interface relation for the twist boundary is  $(10\bar{1}0)_1 \parallel (10\bar{1}0)_2, [0001]_1 \parallel [1\bar{2}10]_2$  and for the tilt boundary  $(0001)_1 \parallel (1\bar{2}10)_2, [10\bar{1}0]_1 \parallel [10\bar{1}0]_2$ .

WC(0001)  $\parallel$  Co(001) orientation [55]. In Paper III, the energetics of these special WC/Co interfaces are examined.

### 2.1.5 Additions

Various transition metals from group IV-B to VI-B in the periodic system are often added to the WC-Co system either as metal or carbide powder. By the addition of strong cubic carbide formers (TiC, ZrC, NbC, HfC and TaC), a mixed cubic  $(M,W)C_x$  phase ( $M = \text{Ti, Nb, etc.}$ ), denoted  $\gamma$ -phase, will form during sintering. The  $\gamma$ -phase formers are usually added in such large proportion that  $\gamma$ -phase is retained throughout the sintering. If not all cubic carbide has been in solution during sintering, the  $\gamma$ -phase grains will have a core of  $MC_x$ , whereas the rim, which grows in equilibrium with WC, will have a mixed  $(M,W)C_x$  composition.

The presence of cubic carbide grains improves the hardness and compressive strength of the hardmetal at high temperatures, and these type of grades are therefore used for high-speed machining of steel [3]. However, the effects of cubic carbides at high temperatures are not unequivocally positive. In a study of deformed WC-Co with TaC additions, it was observed that TaC provides improved resistance against plastic deformation at temperatures around  $1000^\circ\text{C}$ , which can be explained by the higher hardness of cubic  $(\text{Ta,W})C$  grains compared to that of WC grains [56]. At temperatures around  $1200^\circ\text{C}$ , the TaC-containing material actually performed worse than straight WC-Co, which was attributed to easier sliding of  $\alpha/\gamma$  boundaries than  $\alpha/\alpha$  boundaries [56]. The chemical stability of the cubic carbides makes  $\gamma$ -containing hardmetals less prone to diffusion wear, where the wear mechanism depends on the solubility of the tool material in the chip material flowing over the insert. However, the application of coatings reduces the wear of the tool, and the metal removal rate is today often limited by the resistance of the tool against deformation [3]. The advantage of including a second carbide phase would then mainly lie in the fact that it introduces more material variables, as e. g. grain sizes of the  $\alpha$ - and  $\gamma$ -phases can be varied independently, which allows tailoring of gradient structures.

Additions of especially VC are made to inhibit WC grain growth, but also TiC, Cr<sub>3</sub>C<sub>2</sub>, NbC and TaC alone or in combination can be used as growth inhibitors [9, 3]. At typical doping levels for growth inhibition, the amounts of V and Cr are so small that these atoms are completely dissolved in the binder at liquid phase sintering temperatures. Typically during the cooling stage, Cr will not form a separate carbide phase but remains in the binder, whereas V precipitates into a mixed (V,W)C<sub>x</sub> phase [17]. The inhibition effect does not increase once the solubility limit in the binder is reached [57].

The addition of inhibitors, which can be made already during WC powder production, becomes increasingly important to successfully retain the structure of finer powder in the sintered material. The fine materials (of submicron < 1 μm and ultra-fine < 500 nm grain sizes) have many advantageous mechanical properties as high hardness, wear resistance and compressive strength, and find applications as e. g. micro-drills in the electronic industry, dental drills and wear parts [3]. Due to an inverse proportionality between hardness and toughness, fine grades are less tough than coarser grades, but it has been speculated that the hardness-toughness relationship may change for true nanoscale materials with grain sizes below 30 nm possibly allowing hardness increase without sacrificing toughness [10]. Such materials remain to be produced and explored.

Although the effect of grain growth inhibitors is well-known in practice, the atomic mechanism behind the inhibition remains to be clarified. Generally, grain growth is driven by the reduction of interface energies [58]. Although the mechanism of WC growth is complex especially in the early stages of sintering and for nano-sized powder [59], it is usually recognized that WC growth occurs by dissolution-reprecipitation processes (see the discussion in Ref. [17]). In the classic Ostwald ripening process, atoms from small grains dissolve and diffuse towards large grains, where they reprecipitate with a resulting net lowering of the interface energy [60]. In the WC-Co system, WC growth is regarded as being limited not by diffusion in the binder but by the interfacial reactions occurring at WC/WC and WC/Co boundaries [61, 15, 17].

Compared to other metal-ceramic systems, grain growth in WC-Co is slow [61, 9, 17], which can be linked to the faceted WC shape in Co and the atomically sharp interfaces [62]. At a sharp solid/liquid interface two growth modes are possible: 2D nucleation and growth or defect-assisted growth [63, 62, 64, 65, 66]. In the former growth mode, growth is limited by the creation of a nucleus on the otherwise flat surface. Once the nucleus has overcome a critical size, growth parallel to the surface proceeds comparatively fast and is limited by the diffusion of atoms to the advancing growth edge [63]. In the latter growth mode, defects at the solid/liquid interface, e. g. protruding dislocations or stacking faults, create growth sites. Comparison of grain size distributions in materials sintered from milled and unmilled WC powders indicates that defects introduced during milling affect the WC grain growth [62].

Regardless of growth mode, grain growth inhibitors likely interfere with the precipitation step [9, 17] – not dissolution as W diffusion into Co is rapid [67, 17]. This would require a segregation of inhibitor atoms either to WC surfaces or, more

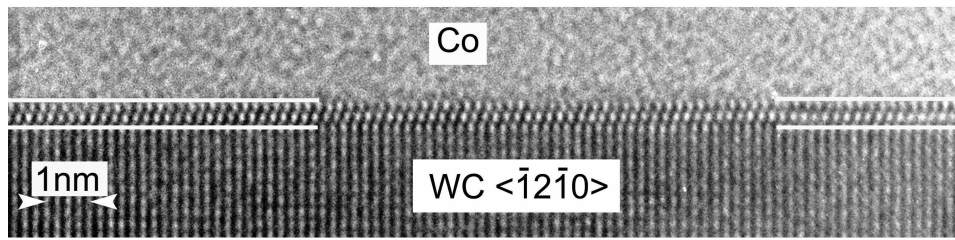


**Figure 2.9:** An HREM image showing an ultrathin cubic film with a thickness corresponding to 2–3 V layers lying between the WC(0001) surface and the Co binder phase. The cubic VC film and WC surface are related with  $(0001)_{\text{WC}} \parallel (111)_{\text{VC}}$  and  $[\bar{1}2\bar{1}0]_{\text{WC}} \parallel [\bar{1}10]_{\text{VC}}$  [70]. Courtesy of S. Lay.

concentrated, to active growth sites as interfacial defects and edges. Jaroenworoluck *et al* used energy dispersive x-ray spectroscopy (EDS) in the TEM and observed a strong V segregation tendency to WC{0001} surfaces and weaker segregation to WC{10 $\bar{1}$ 0} surfaces in VC-doped WC-Co [35, 68]. By high-resolution electron microscopy (HREM) it was also observed that the morphology of the WC grains changes due to VC-doping, so that interfaces become faceted and consist of fine multisteps in contrast to the otherwise straight interfaces of undoped WC-Co [35, 68]. Further detailed HREM imaging by Yamamoto *et al* showed that WC{0001} surfaces in liquid-phase sintered VC-doped WC-Co are covered by a few atomic layers thick precipitates, which were supposed to be of  $(\text{V,W})_2\text{C}$  structure [69]. Atomically thin films in WC/Co interfaces were seen also in HREM imaging by Lay *et al* in both VC-doped and VC + Cr<sub>3</sub>C<sub>2</sub>-codoped materials. By considering the atomic stacking of the films, these were identified with the cubic  $(\text{V,W})\text{C}_x$  phase [70]. Cubic films were primarily detected at basal WC surfaces, but, albeit thinner, sometimes at prismatic surfaces [70]. In the VC + Cr<sub>3</sub>C<sub>2</sub>-codoped WC-Co, films with M<sub>2</sub>C and more complex stackings have also been seen at basal WC/Co interfaces [71]. An HREM image of a typical WC/Co interface in VC-doped WC-Co is given in Figure 2.9.

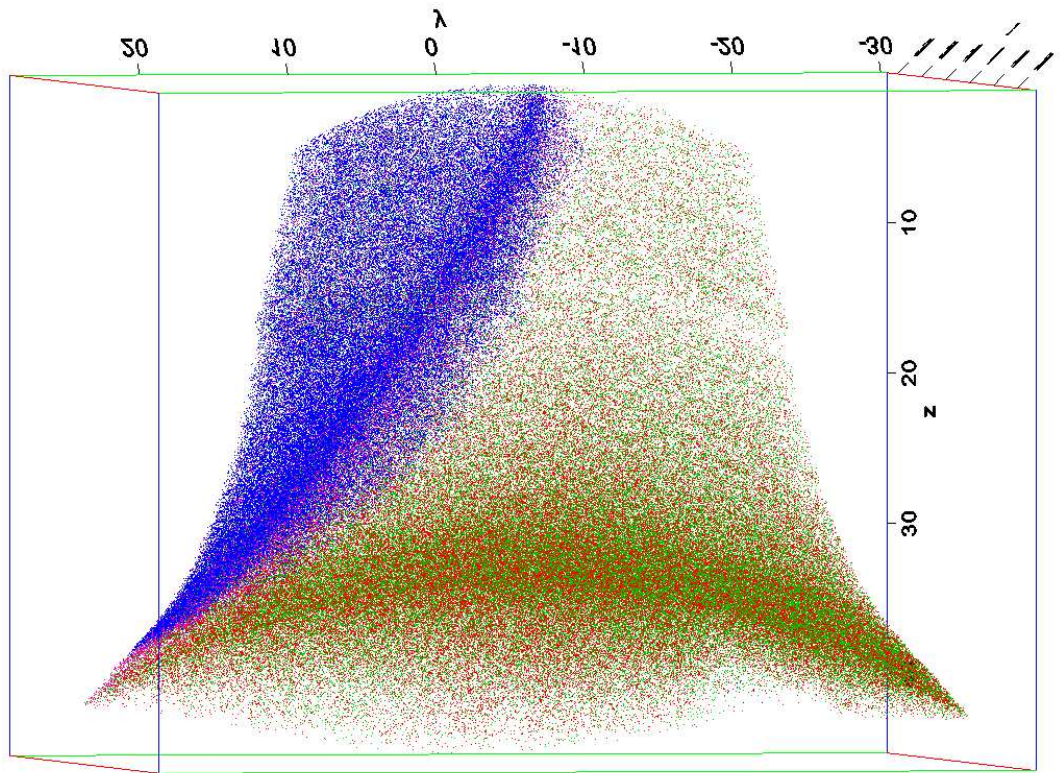
The structure of interfacial films has been well characterized, but the chemical composition of the film is difficult to examine experimentally. Composition is usually acquired by EDS measurements, which can give information about atomic concentrations in the interface relative to the bulk of the binder. However, the effective beam diameter, i. e. the diameter from which the characteristic X-rays of elements are emitted, is in the nanometer-range [72] and would thus simultaneously cover the WC phase, the film and Co binder.

Better resolution is provided by the atom-probe tomography (APT) technique. In APT, atoms in a sharp tip specimen are field evaporated as ions by laser or voltage pulses, accelerate in an electric field and hit a position-sensitive detector. Using time of flight, from which the mass over charge ratio of the ion is determined, and  $x, y$  coordinates from the detector allows a complete 3D reconstruction of the specimen with a spatial resolution in the Å range [73]. An example of an image from APT of a WC/Co interface in VC-doped WC-Co is given in Figure 2.10. The amount

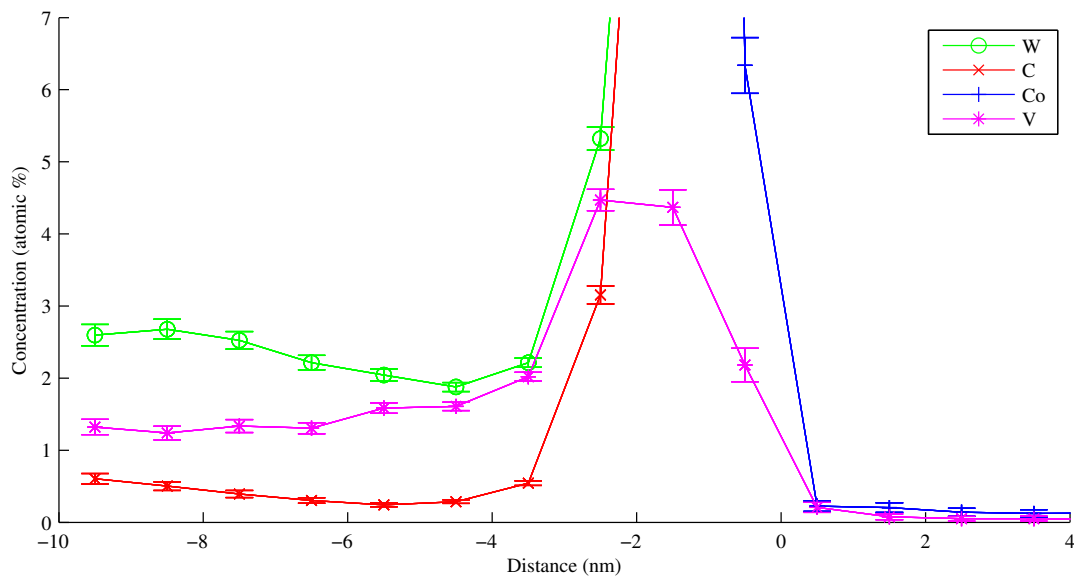
of segregated V at the interface in the image corresponds to 1.0 to 1.3 complete V monolayers. The variation depends on the assumed atomic density in the interface plane, which is unknown as the orientation of the WC phase and the film with respect to the interface plane is undetermined.

In literature, there is no unanimous description of the role of the interfacial films in the growth inhibition mechanism. Jaroenworoluck *et al* suggest that accumulation of V at the fine steps at the interface hinder the movement of the WC migration front [35]. Lay *et al* assume that the interfacial films form barriers for W diffusion into or out of WC grains, and thereby suppress WC growth in directions perpendicular to the plane of the film [71]. Kawakami *et al* studied V segregation in WC-Co specimens cooled in two ways: usual cooling in the furnace and rapid cooling in a water bath [72, 74]. It was found that the amount of segregated V at WC/Co interfaces was smaller and that interfacial films were thinner in the rapidly cooled specimen. Although interfacial V-rich layers were seen to exist also in the rapidly cooled specimen, the authors concluded that the layers themselves were not responsible for the growth inhibition but precipitate during cooling from the liquid-phase, and proposed that the inhibition effect of V is caused by intermittent adsorption and desorption of V atoms to atomic-sized steps at WC/Co interfaces [72, 74]. However, V segregation at WC/Co interfaces is evident in solid-state sintered WC-Co [69] and VC is a very effective inhibitor of growth in the earliest stages of sintering [19, 59]. The question under what conditions VC films can exist in WC/Co interfaces is addressed in Paper I, where we study the stability of atomically thin films of VC in WC(0001)/Co interfaces.

From available comparisons [75, 76, 77], it is clear that the propensity of formation of films at WC/Co interfaces is largest in VC-doped WC-Co. As for VC-doping, films at both basal and prismatic interfaces have been seen in Cr<sub>3</sub>C<sub>2</sub>-doped WC-Co [78]. In TiC-doped WC-Co, films exist only at WC{0001} surfaces [75]. Although carefully examined, interfacial films were not detected in ZrC- [76, 77], NbC- [76] or TaC-doped [75] WC-Co. Under the assumption that these observations have bearing to the situation during sintering, it is interesting to compare with morphological features of the as-sintered microstructure of doped WC-Co. As an example, Ti-doping can be used to induce the formation of platelet-like WC grains in WC-Co [79] (and also in WC-Ni [80]), which has been ascribed to a defect-assisted growth arising from the presence of cubic layers on WC{0001} surfaces inside WC grains [79]. Within the scope of this project, it has been found that TiC in comparison with ZrC, NbC and TaC is an effective WC growth inhibitor [45]. Further discussion is given in Paper II, where we have calculated the propensity of film formation in different WC/Co interfaces for various cubic carbides and compared with available experimental results.



(a)



(b)

**Figure 2.10:** (a) A reconstruction of a WC/Co interface in V-doped WC-Co from atom probe tomography. (b) The concentration across the interface. The binder is to the left. Courtesy of J. Weidow.

## 2.2 Steels

Steels represent not only the most widely used metallic materials, but also perhaps the most complex group of alloys. Despite the mechanical weakness of pure iron, steels show a diversity in mechanical properties with yield stresses spanning from 200 MPa to 5500 MPa [81]. The common feature in steel production is the addition of carbon to iron. Such low concentrations of carbon as 0.5 atomic percent have a decisive strengthening effect on iron.

As suggested in the 1930s independently by Taylor, Orowan, and Polanyi, plastic deformation in many crystals occurs by slip mediated by the movement of dislocations. Compared to Fe atoms, C atoms have such small atomic size that they usually become interstitial solute atoms of high diffusivity. Due to the mismatch in size with the surrounding matrix, the solute atoms will give rise to an elastic field and are likely to be found in the vicinity of dislocations, where the distorted lattice provides room for favorable interstitial sites. Effectively, the C atoms act as hinders for the dislocation movement thus increasing the hardness of the metal.

Several other important strengthening methods exist. Grain boundaries limit the mean free path for the dislocation making a fine-grained material more likely to resist plastic deformation. However, at least for incoherent boundaries, the resistance against grain boundary sliding is low and this mode of plastic deformation may dominate a fine-grained material. During work hardening, the metal undergoes mechanical work of high enough frequency and magnitude to not only move dislocations, but also to create new ones. The created dislocations entangle and lock each other. Too aggressive hardening will, however, make the material brittle, since the lack of mobile dislocations will instead induce the formation of cracks when the material is set under tension.

The strengthening mechanism motivating the work in Papers V and VI is precipitation formation. The first step of this strengthening process is to form a solid solution of carbon, nitrogen, and other metallic alloying elements. Cooling will lead to a supersaturation of the solid solution and during a subsequent application of an appropriate heat treatment, excess solutes will precipitate to form a second phase. Examples of precipitates are  $M_{23}C_6$ , MX, and  $M_2X$ , where M is a metal atom and X is C or N [81].

The role of the precipitates is to act as obstacles for gliding dislocations. If a dislocation moving along its glide plane encounters a precipitate, it can proceed by cutting through the particle or avoid it by bowing out around the particle, eventually leaving a dislocation loop around the precipitate [82]. At higher temperatures, thermally activated diffusion of atoms may allow the dislocation to climb and continue gliding past the precipitate. The processes by which the dislocations can avoid the obstacle all require energy and therefore enhances the strength of the material.

In Papers V and VI, the nacl VN phase is studied. In steels, VN precipitates as small discs of nacl structure within the bcc-Fe matrix. A HREM study of VN precipitates in steels has been done by Bor *et al* [83], which clearly shows the disc-like structure of VN. The flat side of the disc shows a misfit of only 2% with the

surrounding Fe matrix, which gives an experimentally well established interface structure of Baker-Nutting relation  $(001)_{\text{nacl}} \parallel (001)_{\text{bcc}}, [100]_{\text{nacl}} \parallel [110]_{\text{bcc}}$ . As was shown in HREM imaging, the misfit is taken up by misfit dislocations [83]. The side of the disc is incoherent with the matrix.

The formation process of precipitates is directly dependent on the interface energy between the precipitate and the matrix, since it governs the rate of nucleation and growth. An understanding of these processes is essential to predict long-term structural changes in steel, or, more specifically, its creep resistance, i. e. its ability to withstand stress applied during a long time period.



## Computational methods

This chapter describes the computational methods used in the appended papers. The bulk part of the work has been performed in the framework of density functional theory (DFT), which is a first-principles theory capable of accurately predicting materials properties without introducing empirical parameters or major simplifications. DFT has today become the standard workhorse of the solid-state physicist and all appended papers include results of DFT calculations. A short background of the theory is given in Section 3.1.1.

DFT deals on a rather detailed level with the electronic and atomic structure of the material and is thus associated with a high computational price and limited to small system sizes. By omitting the direct correspondence to electronic structure, simpler atomic model potentials provide faster calculations which can be used to study extended material defects. This is done in Paper V, where we use the embedded atom method (EAM) to study interfacial misfit dislocations. EAM is described in Section 3.2. Omitting also the atomic structure, an even simpler continuum description is obtained, which we use in the form of anisotropic elasticity theory in Papers V and VI. Elasticity theory is described in Section 3.3.

To obtain a complete microscopic description of a physical system, a determination of the quantum mechanical ground state accounting for both nuclear and electronic degrees of freedom must be made. The first step towards a tractable atomistic description is usually (with a notable exception in Car-Parrinello quantum molecular dynamics) the Born-Oppenheimer approximation [84], under which the many-body wavefunction including both electrons and nuclei is separated into an electron and a nuclear part. Because of the large ratio between the nucleus and electron masses, the electrons will almost instantaneously adapt to a change in nuclear positions, and the nuclei will hence move on the potential energy surface given by the electronic ground state. The total energy can thus be written

$$E = E(\vec{R}_\alpha), \tag{3.1}$$

where  $\vec{R}_\alpha$  is a set of all atomic coordinates of the system.

Basically, there are two different ways of deriving the potential  $E(\vec{R}_\alpha)$ . The most fundamental is the first principles method, which ideally gives  $E(\vec{R}_\alpha)$  with no other input than the atomic species and positions. It is often a reliable, yet computationally demanding method. The alternative is to estimate  $E(\vec{R}_\alpha)$  semiempirically, where a functional form for the potential is guessed from physical reasoning and parameters are fitted to experiments and/or first-principles calculations.

### 3.1 First-principles calculations

At the basis of any first-principles method lies the time-independent Schrödinger equation, which, under the Born-Oppenheimer approximation, takes the form

$$H\Psi(\vec{r}_\beta; \vec{R}_\alpha) = E(\vec{R}_\alpha)\Psi(\vec{r}_\beta; \vec{R}_\alpha), \quad (3.2)$$

where  $\Psi$  is the electronic wavefunction. The set of electronic coordinates is denoted  $\vec{r}_\beta$  and explicit reference is made to the fact that the energy and wavefunctions are only parametrically dependent on the nuclear coordinates  $\vec{R}_\alpha$ . The Hamiltonian consists of three parts

$$H = T + V_{ee} + V_{\text{ext}}, \quad (3.3)$$

where  $T$  is the kinetic energy,  $V_{ee}$  the electron-electron interaction, and  $V_{\text{ext}}$  the potential from the nuclei including also the constant energy shift due to the Coulomb interaction between the nuclei themselves. According to the variation principle, the ground state energy  $E$  can be found by finding the minimum

$$E = \min_{\Psi} \langle \Psi | T + V_{ee} + V_{\text{ext}} | \Psi \rangle, \quad (3.4)$$

where the minimization is over all antisymmetric  $N$  electron wavefunctions  $\Psi$ .

For a piece of real material containing an Avogadrian number of particles, solutions to the Schrödinger equation are computationally not feasible. In fact, only a handful electrons can be treated exactly. The problems arise from the electron-electron interaction  $V_{ee}$  which renders a decomposition of the total wavefunction into a product of one-particle wavefunctions impossible. An approximate treatment or neglect of electron-electron interaction is therefore a common feature of many electron structure calculations.

In the Hartree-Fock (HF) method, the minimum in Eq. (3.4) is sought among anti-symmetrized (in spin and space coordinates) products of one-particle wavefunctions. Thus, by construction the HF method incorporates an exact treatment of the exchange effect, i. e. the solution fulfills the Pauli principle stating that two or more fermions cannot occupy the same state. The coulombic electron-electron interaction is however approximated in a mean-field approach by the Hartree energy\*

$$E_{\text{H}}[n] = \frac{1}{2} \int \int d\vec{r} d\vec{r}' \frac{n(\vec{r})n(\vec{r}')}{|\vec{r} - \vec{r}'|}, \quad (3.5)$$

---

\*In this chapter, units are chosen so that  $\hbar = m_e = e = 1$ .

where  $n(\vec{r})$  is the electronic charge density. The difference between the exact ground state energy and the HF energy can be defined as the correlation energy and stems from the all Coulomb interaction between electrons not accounted for by Eq. (3.5). Extensions to the HF scheme are possible, e. g. by expanding the basis set with one-particle wavefunctions of higher excitations [85]. However, with increasing system size the computational burden of the HF method quickly makes this approach unfeasible.

### 3.1.1 Density functional theory

Fundamentally, there are two choices of variable for characterizing an electronic system in the ground state: the wavefunction or the electronic density. Relying on the electron density of 3 coordinates rather than the many-particle wavefunction of  $3N$  coordinates, DFT is an obvious choice for the treatment of large systems. DFT is, in principle, capable of treating the electron-electron interaction exactly, but in practice it must be approximated and its applicability depends strongly on the accuracy of these approximations. In this section, some basics of DFT are given.

Since its formulation in the 1960s, DFT has become one the most successful computational methods in atomistic calculations. A thorough introduction is given by Martin [85]. The basis of DFT is formed by two theorems of Hohenberg and Kohn [86]. The first Hohenberg-Kohn theorem states that the electron density may be used in place of the potential as the basic function uniquely characterizing the system, or in other words, the ground state density  $n(\vec{r})$  uniquely determines the external potential  $V_{\text{ext}}(\vec{r})$  up to an arbitrary constant.

By defining a functional

$$F[n] = \min_{\Psi \rightarrow n} \langle \Psi | T + V_{\text{ee}} | \Psi \rangle, \quad (3.6)$$

where the minimization is over all antisymmetric wavefunctions  $\Psi$  that gives a particular density  $n$ , the search in Eq. (3.4) can be reformulated into

$$E = \min_n \left( F[n] + \int V_{\text{ext}}(\vec{r})n(\vec{r}) d\vec{r} \right), \quad (3.7)$$

where the minimization is over all  $N$  electron charge densities  $n$  [87]. Now, the second Hohenberg-Kohn theorem states that there exists a single universal functional  $F[n]$ , i. e. it is independent of the external potential. By introducing a functional  $E[n]$  defined as in Eq. (3.7) excluding the minimization and a Lagrange multiplier  $\mu$  for the fixed particle number constraint,

$$N = \int d\vec{r}n(\vec{r}), \quad (3.8)$$

one seeks to minimize  $E[n] - \mu N$  through the Euler-Lagrange equation

$$\frac{\delta F}{\delta n(\vec{r})} + V_{\text{ext}}(\vec{r}) = \mu. \quad (3.9)$$

This would be a convenient way of determining the ground state properties of any external potential if only the functional  $F[n]$  was known. It is, however, not and the importance of the Hohenberg-Kohn theorems could therefore seem to be primarily theoretical.

Fortunately, Kohn and Sham [88] found a mathematically tractable way of solving the original many-body problem. In the Kohn-Sham formulation, the starting point is to separate  $F[n]$  into different parts,

$$F[n] = T_s[n] + E_H[n] + E_{xc}[n], \quad (3.10)$$

where  $T_s[n]$  is the kinetic energy functional for *non-interacting* electrons, and  $E_H[n]$  is the Hartree energy (3.5).

The remaining term of Eq. (3.10),  $E_{xc}[n]$ , is called the exchange-correlation energy, which should capture all errors arising from replacing  $T + V_{ee}$  by  $T_s + E_H$ . The essential result of the Kohn-Sham formulation is that the Euler-Lagrange equation (3.9) for the functional (3.10) is *exactly* fulfilled for a set of non-interacting electrons obeying the one-electron Schrödinger equation (in atomic units),

$$\left( -\frac{1}{2}\nabla^2 + V_{KS}(\vec{r}) \right) \phi_i(\vec{r}) = \varepsilon_i \phi_i(\vec{r}) \quad (3.11)$$

where  $V_{KS}$  is a density-dependent potential, given by

$$V_{KS}(\vec{r}) = V_{\text{ext}}(\vec{r}) + \frac{\delta E_H[n(\vec{r})]}{\delta n(\vec{r})} + \frac{\delta E_{xc}[n(\vec{r})]}{\delta n(\vec{r})}. \quad (3.12)$$

From a comparison of Eq. (3.10) and Eq. (3.11) it is deduced that

$$E = \sum_i f_i \varepsilon_i - E_H[n(\vec{r})] + E_{xc}[n(\vec{r})] - \int d\vec{r} n(\vec{r}) \frac{\delta E_{xc}[n(\vec{r})]}{\delta n(\vec{r})}, \quad (3.13)$$

where  $f_i$  is the occupational number of the electronic Kohn-Sham state  $i$ . To find the energy  $E$  in practice, one has to solve the Kohn-Sham equation (3.11) iteratively, since  $V_{KS}$  depends on the solution itself. Starting with a reasonable first guess for the density, the equations are solved till self-consistency.

Some points are worth noting. In principle, the Kohn-Sham equations are exact and yield the exact density. Since the equations are single-particle equations, they are much easier to solve than the originally coupled Schrödinger equation. In return, however, the electron-electron interaction energy has to be approximated. By separating the interaction into  $E_H[n]$  and  $E_{xc}[n]$ , where the former is known exactly, it turns out that the latter is amenable to efficient approximations.

A physically transparent view of the exchange-correlation energy can be gained by considering the so-called adiabatic connection formula [89]. Imagining that the electron-electron interaction were gradually increased from 0 to the real Coulomb interaction  $1/|\vec{r} - \vec{r}'|$  with a factor  $0 < \lambda < 1$ ,  $E_{xc}[n]$  can be written

$$E_{xc}[n] = \frac{1}{2} \int d\vec{r} n(\vec{r}) \int d\vec{r}' \frac{1}{|\vec{r} - \vec{r}'|}, n_{xc}(\vec{r}, \vec{r}') \quad (3.14)$$

where

$$n_{xc}(\vec{r}, \vec{r}') = n(\vec{r}) \int d\lambda [g(\vec{r}, \vec{r}', \lambda) - 1]. \quad (3.15)$$

$g(\vec{r}, \vec{r}', \lambda)$  is a pair correlation function for the system of density  $n(\vec{r})$  and electron-electron interaction  $\lambda/|\vec{r} - \vec{r}'|$ . A physical interpretation of Eq. (3.14) is that the exchange-correlation energy  $E_{xc}$  originates from the interaction energy between an electron at  $\vec{r}$  and the density  $n_{xc}(\vec{r}, \vec{r}')$  of an electron hole that it creates due to the Pauli principle and the Coulomb repulsion.

### Exchange-correlation approximations

A first approximation of  $E_{xc}[n]$  was suggested already in the original Kohn-Sham paper [88] and is known as the local density approximation (LDA). In the LDA, the exchange-correlation energy at a point  $\vec{r}$  is set equal to the exchange-correlation energy  $\epsilon_{xc}(n)$  of a homogeneous electron gas of density  $n(\vec{r})$ , making

$$E_{xc}[n] = \int d\vec{r} n(\vec{r}) \epsilon_{xc}(n(\vec{r})). \quad (3.16)$$

For the homogeneous electron gas, an exact expression can be derived for the exchange energy  $\epsilon_x$  by calculating a Fock integral for a Slater determinant of orbitals. This motivates the splitting of exchange-correlation energy into two parts:  $\epsilon_{xc} = \epsilon_x + \epsilon_c$ . The correlation part  $\epsilon_c$  can be found from Monte Carlo simulations [90].

LDA has proven to be a surprisingly good approximation for exchange and correlation, at least in solids. The reason is that exchange and correlation effects are short-ranged and one can therefore expect that LDA will work best for solids resembling a homogeneous gas and worst for inhomogeneous systems, like free atoms or molecules. However, LDA also works for some cases of varying density, which is considered to be a consequence of the fact that its exchange-correlation hole satisfies some conditions for an exact hole, e. g.  $\int d\vec{r}' n_{xc}(\vec{r}, \vec{r}') = -1$  and other sum rules [89].

To better deal with inhomogeneous systems, a more elaborate exchange-correlation approximation should extend the LDA and include also semilocal contributions to the energy. A procedure to include  $|\nabla n|$  was suggested already in the original Kohn-Sham paper [88]. However, a straight-forward gradient expansion approximation (GEA) of low-order of the exact exchange-correlation energy tend to give worse results than LDA as the GEA violates certain conditions of the exchange-correlation hole, e. g. the sum rules [85]. Instead, generalized gradient approximations (GGA) have been introduced, where the exchange-correlation energy takes the form

$$E_{xc}[n] = \int d\vec{r} n(\vec{r}) \epsilon_{xc}^{GGA}(n(\vec{r}), \nabla n(\vec{r})). \quad (3.17)$$

In contrast to LDA, there is no unique definition of  $\epsilon_{xc}^{GGA}(n, \nabla n)$  and a diversity of functionals has developed.

In Paper V and VI, the GGA version by Perdew and Wang (PW91) [91] has been used. In Paper I to IV, we have instead used the functional of Perdew, Burke and Ernzerhof (PBE) [92], which is probably the most commonly used functional for solid-state calculations today. PW91 and PBE usually produce similar results for lattice constants, bulk moduli and atomization energies, but can differ substantially where large density gradients appear as for vacancies and surfaces [93]. As this thesis mostly deals with dense phases and interfaces, the PBE functional should be appropriate. However, for surfaces an extension to PBE, called PBEsol, has recently been suggested [94]. The PBEsol functional has been adjusted to give better predictions of surface energies at the expense of atomization energies. Surface energies in PBEsol are generally higher than in PBE, thus improving on the too small surface energies of PBE [95]. For future studies of the systems considered in this thesis, PBEsol should therefore be a good choice of functional.

### Plane-wave implementation

After the simplification introduced by the Kohn-Sham approach to DFT, one is still left with the problem of actually solving the Kohn-Sham equations for all electrons of the system. For isolated atoms and molecules the Kohn-Sham states are usually expanded using localized basis sets. For solids, however, the natural choice of basis set is plane waves. Consequently, periodical boundary conditions are imposed on the computational cell. Then, the conditions for Bloch's theorem are fulfilled, meaning that the wavefunctions can be written as

$$\Psi_{n,\vec{k}}(\vec{r}) = u_{n,\vec{k}}(\vec{r})e^{i\vec{k}\cdot\vec{r}}, \quad (3.18)$$

where  $u_{n,\vec{k}}(\vec{r})$  has the periodicity of the lattice,  $n$  is the band index, and  $\vec{k}$  is a vector in the first Brillouin zone. Due to the periodicity,  $u_{n,\vec{k}}(\vec{r})$  can be expanded in plane waves with wave vectors of the reciprocal lattice,

$$u_{n,\vec{k}}(\vec{r}) = \sum_j c_{n,\vec{k},j} e^{i\vec{G}_j\cdot\vec{r}}. \quad (3.19)$$

To create a finite basis set, only reciprocal lattice vectors of kinetic energy  $|\vec{k} + \vec{G}|^2 / 2 < E_{\text{cutoff}}$ , where  $E_{\text{cutoff}}$  is some predefined cutoff, are included in the sum. The easily tunable parameter of accuracy  $E_{\text{cutoff}}$  is, in practice, an advantageous feature of a plane waves basis.

The electron density is given by an integration over the first Brillouin zone

$$n(\vec{r}) = \sum_j \int_{\text{1BZ}} d\vec{k} f_{j\vec{k}} |u_{n,\vec{k}}(\vec{r})|^2 \quad (3.20)$$

where  $f_{j\vec{k}}$  is an occupancy factor for state  $j\vec{k}$ . In practice, the integral (3.20) is replaced by a sum over certain  $\vec{k}$ -vectors. Usually these  $\vec{k}$ -vectors are set in a uniform grid as in the Monkhorst-Pack scheme [96]. Ideally at  $T = 0\text{ K}$ , the occupancy

$f_{j\vec{k}} = 2\theta(\epsilon_F - \epsilon_{j\vec{k}})$ , i. e. all states are completely filled up to Fermi level  $\epsilon_F$ . However, in metallic systems with a finite density of states at  $\epsilon_F$ , it is for numerical reasons necessary to smear out the discontinuity of the occupancy. In the papers, the smearing method of Methfessel and Paxton is used [97].

In practical DFT calculations, energy cutoff,  $\vec{k}$ -point grid and smearing parameter are the most frequently used “knobs” fiddled with to achieve the desired technical accuracy. Experience helps in choosing good starting values of the parameters for new systems and geometries.

### Pseudopotentials

The drawback of using a delocalized basis set such as plane waves, is the need of a large basis set to accurately describe localized functions, such as the charge density in the vicinity of the nucleus. However, under reasonable conditions, the core electron states are often negligibly affected by the atomic environment, and only valence electrons contribute appreciably to chemical bonding. To reduce the number of necessary plane waves, the effect of core electrons and nucleus is accounted for implicitly by a pseudopotential. The pseudopotential is constructed so that the true all-electron wavefunction and the pseudo-wavefunction coincide outside some appropriately chosen core radius  $r_c$ . Using this construction, the often complicated structure of the true wavefunction inside  $r_c$  can be simplified into a smoother pseudo-wavefunction.

The pseudopotentials used in this work are of Blöchl’s project augmented wave (PAW) form [98] as implemented by Kresse and Joubert [99]. The construction of pseudopotentials involves many technicalities and the reader is referred to Ref. [85] or the aforementioned references for details.

## 3.2 Semiempirical methods

Although bonding between atoms is of quantum mechanical origin, where electrons act as a glue between the positively charged nuclei, it is often desirable to remove the explicit dependence of the electrons on the total energy, and only consider the energy as a function of atomic coordinates, where the electrons are effectively integrated into the energy function  $E(\vec{R}_\alpha)$ .

The simplest example of an energy function  $E(\vec{R}_\alpha)$  takes the form

$$E = \sum_{\substack{i,j \\ i < j}} V(R_{ij}), \quad (3.21)$$

where  $V$  is a pair potential and  $R_{ij}$  is the distance between atom  $i$  and  $j$ . The total energy is here decomposed into contributions from interactions between pair of atoms. The most familiar and thoroughly investigated pair potential is the Lennard-Jones potential, where

$$V(R_{ij}) = 4\epsilon \left[ \left( \frac{\sigma}{r} \right)^{12} - \left( \frac{\sigma}{r} \right)^6 \right]. \quad (3.22)$$

$\varepsilon$  is the depth of and  $\sigma$  the distance where the potential changes sign from repulsive to attractive. The potential can be used to study systems of closed-shell atoms, where interaction occurs mainly due to polarization.

The advantage of pair potentials is the ability to quickly calculate total energies and forces. Hence they are attractive for molecular dynamics simulations and thermodynamical calculations. The physical justification of their use is however weak and the problems are both qualitative and quantitative. As an example of the former, the energy of a bond between two atoms will always be the same, regardless of the environment. Quantitatively, pair potentials cannot accurately describe even the simple case of elastic deformation of a solid. Described by pair potentials, a material of cubic symmetry will always fulfill the so called Cauchy relation,  $c_{12} = c_{44}$ , for its elastic constants.

### Embedded atom method

To remedy some of the shortcomings of pair potentials, it is necessary to account for the environmental dependence of the bond strength. This can be accomplished by including an additional term to the total energy function,

$$E = \sum_{\substack{i,j \\ i < j}} V(R_{ij}) + \sum_i F(\rho_i), \quad (3.23)$$

where the physical interpretation and expression for  $F(\rho_i)$  varies among different workers. This functional form was used extensively in the 1980s to predict properties of defects in solids, and has appeared with different names such as Finnis-Sinclair potential [100], effective medium theory [101] (EMT), and embedded atom method [102] (EAM).

The Finnis-Sinclair potential is derived from a tight-binding model. By utilizing information about the second moment  $\mu_2$  of the local density of states, it turns out that  $F(\rho_i)$  is proportional to the square root of  $\mu_2$ . It is further argued that  $\mu_2$  can be taken as a sum of pairwise interactions between neighboring atoms, which leads to a functional form  $F(\rho_i) \propto \sqrt{\rho_i}$ , where  $\rho_i$  is given by an expression similar to Eq. (3.24) below.

The physical idea behind the EMT and EAM is that there is a certain energy cost  $F(\rho_i)$  associated with placing an atom in an electron gas. If one considers a metal in a periodic structure, one can think of one particular atom  $i$  as being embedded in the electron density  $\rho_i$  given by the rest of the atoms. In EMT,  $F(\rho_i)$  can be determined explicitly from DFT by calculating the energy of placing an atom in jellium at density  $\rho_i$ . In EAM, however,  $F(\rho_i)$  is determined semi-empirically and the density at atom  $i$  is taken to be a sum

$$\rho_i = \sum_{j \neq i} f(R_{ij}). \quad (3.24)$$

of contributions  $f(R_{ij})$  from its neighbors.

By combining a pair potential to describe the Coulombic interaction between the nuclei with an embedding energy for the electron gas, EAM has successfully been used for modeling metals of non-directional bonding. From a computational point of view, EAM is only twice as time-consuming as a simple pair potential. In Paper V, an EAM implementation for Fe [103] has been used to calculate the elastic energy of misfit dislocations. In this implementation, the energy function is fitted to cohesive energy, lattice parameter, elastic constants, vacancy formation energy and adjusted to fit Rose's zero temperature equation of state [104].

### 3.3 Elasticity theory

Elasticity theory is a versatile theory applicable to such different problems as understanding crystal defects to constructing bridges and thus spans a range of length scales from nanometers to meters and beyond. Treating a crystal as an elastic body effectively reduces all microscopic degrees of freedom into a few material parameters, elastic constants, and replaces the discrete positions of atoms by a single displacement field. Elasticity theory is used in Papers V and VI to calculate and derive simple expressions for elastic corrections to semicoherent interface energies. This section is included to present some of the underlying equations for these corrections. Good introductions to the theory are given in Ref. [82] and particularly in Ref. [105].

We start this section by deriving elasticity theory directly from atomistic calculations following Ref. [84]. We assume that the energy  $E(\vec{R}_\alpha)$  is fully known from first-principles. The first step in finding the connection is to expand the energy  $E(\vec{R}_\alpha)$  to second order around its equilibrium value  $E_0$ , giving <sup>†</sup>

$$E = E_0 + \sum_{\alpha} \frac{\partial E}{\partial u_{i\alpha}} u_{i\alpha} + \sum_{\alpha, \beta} \frac{1}{2} u_{i\alpha} \frac{\partial^2 E}{\partial u_{i\alpha} \partial u_{j\beta}} u_{j\beta} + O(u_{i\alpha} u_{j\beta} u_{k\gamma}), \quad (3.25)$$

where  $u_{i\alpha}$  is the displacement of atom  $\alpha$ . Note that the second term of Eq. (3.25) is zero, due to force equilibrium. By assuming that the atomic displacements vary only slightly from lattice site to lattice site, it is possible to consider a continuous displacement field  $\vec{u}(\vec{x})$  that takes the value  $\vec{u}_\alpha$  at lattice site  $\alpha$ , and additionally, under the same assumption,

$$u_{j\beta} = u_{j\alpha} + (R_{j\beta} - R_{i\alpha}) \left. \frac{\partial u_j}{\partial x_i} \right|_{\vec{x}=\vec{R}_\alpha}, \quad (3.26)$$

for nearby  $\alpha$  and  $\beta$ . With these simplifications, the expansion (3.25) reduces to

$$E = E_0 + \frac{1}{2} \sum_{\alpha} u_{j,i} \Big|_{\vec{x}=\vec{R}_\alpha} E_{ijkl} u_{l,k} \Big|_{\vec{x}=\vec{R}_\alpha}, \quad (3.27)$$

<sup>†</sup>Throughout this section, double roman indices imply summation and an index after a comma  $_{,i}$  means differentiation with respect to  $x_i$ .

where

$$E_{ijkl} = - \sum_{\beta} \frac{1}{2} R_{i\beta} \frac{\partial^2 E}{\partial u_{j0} \partial u_{l\beta}} R_{k\beta}. \quad (3.28)$$

In deriving  $E_{ijkl}$ , reference is made to the fact that the atoms are positioned on a Bravais lattice, which makes  $\partial^2 E / (\partial u_{j\alpha} \partial u_{l\beta})$  invariant under a translation of  $\alpha$  and  $\beta$  with a lattice vector. Without a Bravais lattice,  $E_{ijkl}$  would depend on  $\alpha$ .

To proceed, one demands that the energy should be constant for an arbitrary rotation of the material. This implies that the energy depends only on a symmetrical combination  $\epsilon_{ij} = \frac{1}{2}(u_{i,j} + u_{j,i})$ , which is recognized as the linear strain. By replacing the sum (3.27) with an integral, we arrive at an expression for the energy which is usually derived from linear elasticity theory, namely

$$E = E_0 + \int_V \frac{1}{2} \epsilon_{ij} c_{ijkl} \epsilon_{kl} dV, \quad (3.29)$$

where  $V$  is the volume of the crystal and the elastic constants  $c_{ijkl}$  are introduced with the definition

$$c_{ijkl} = \frac{1}{4V} (E_{ijkl} + E_{jikl} + E_{ijlk} + E_{jilk}). \quad (3.30)$$

With the usual approach from elasticity theory, the elastic constants are defined as

$$c_{ijkl} = \left( \frac{\partial^2 e}{\partial \epsilon_{ij} \partial \epsilon_{kl}} \right), \quad (3.31)$$

where  $e$  is the internal energy per unit volume of the body. This can be more rigorously formulated in a proper thermodynamic setting, and if so, the differentiation in Eq. (3.31) should be considered as being performed in an adiabatic process, where the elastic energy stored in the body due to the action of external forces can be completely released upon subsequent removal of the external forces (no dissipation). A corresponding free energy expression defining  $c_{ijkl}$  under constant temperature can also be defined [105]. For a given material, elastic constants can readily be determined from *ab initio* calculations. Experimentally, elastic constants are often measured by acoustic means [106].

The elastic constants determine the response of a linear elastic body to external forces. The quantity  $c_{ijkl}$  is a fourth-rank tensor containing  $3^4 = 81$  elements which relate the nine elements of stress  $\sigma_{ij}$  to the nine elements of strain  $\epsilon_{kl}$  through  $\sigma_{ij} = c_{ijkl} \epsilon_{kl}$ . However, the number of independent elements can be reduced by general arguments to 21 [105]. For crystals, this number is further reduced due to additional geometrical symmetries. E. g. cubic crystals have only three independent elastic constants, whereas hexagonal crystals have five. For back-of-the-envelope calculations, one often makes the further assumption that the medium is elastically isotropic, i. e. the elastic properties are equal in all directions in which case only two independent elastic constants are needed. These constants may be chosen as the shear modulus  $\mu$  and the Lamé constant  $\lambda$  related to the Poisson ratio  $\nu$  by  $\lambda = 2\mu\nu/(1 - 2\nu)$ . In an isotropic medium,  $c_{ijkl} = \mu(\delta_{ik}\delta_{jl} + \delta_{il}\delta_{jk}) + \lambda\delta_{ij}\delta_{kl}$ .

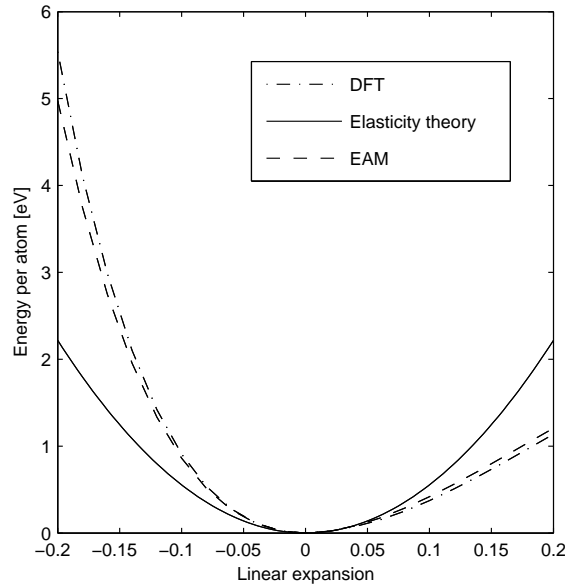


**Figure 3.1:** Elastic energy per atom of a uniformly expanded cell of bcc-Fe as given by different methods.

For a given material, the validity of Hooke's law can be readily tested. In Figure 3.1, the elastic energy of a uniformly compressed and expanded cell of bcc-Fe is given both by DFT and EAM calculations and elasticity theory. We see that the agreement is reasonable up to a few percent of expansion. The plot shows some general deficits of elasticity theory, namely that it usually underestimates energy due to compression, but overestimates energy due to expansion.

### Solving the equations

The basic field equation for the displacement field  $u_i$  is

$$f_i + c_{ijkl}u_{k,lj} = 0, \quad (3.32)$$

where  $f_i$  are body forces (typical examples include gravitational force or electric force on a charged material). To solve a general elasticity problem, Eq. (3.32) coupled to a set of boundary conditions, a finite element method is most often the best choice, and an abundant number of computer codes exist for this purpose. A finite element calculation is included in Paper VI.

In Papers V and VI, we also used analytical expressions for the elastic energy of misfit dislocations. For a special class of anisotropic elastic problems including dislocations and other two-dimensional (plane) problems, a methodology involving complex variables was developed by Eshelby and Stroh [107, 108], the so called sextic formalism. It was later cast into a slightly different form, the integral formalism, by Lothe and coworkers [109, 110, 111]. By applying the theory to a dislocation in an interface, an energy coefficient  $K_{ij}$  can be derived [112].  $K_{ij}$  depends in a

non-trivial way on the elastic constants of the interfacing media and the orientation relationship of the interface and completely determines the elastic response of the interface due to the formation of misfit dislocations (see Paper VI).

## Thermodynamics and modeling of interfaces

Except Paper IV, all appended papers deal with aspects of interfacial energetics. The structure of both inter- and intraphase boundaries are of importance for material properties, and the microstructures that form e. g. during sintering of cemented carbides are to a large degree determined by the thermodynamics of interfaces. Therefore, we start this chapter by introducing the fundamentals of interfacial thermodynamics in Section 4.1.1 and discuss some experimental results of interest to the cemented carbides systems. As a sidetrack, in Paper IV we consider the solubility of transition metals in WC. A short theoretical background on solubility and mixing is given in Section 4.1.3.

The calculation of both absolute interface energies and solubilities requires definite values of thermodynamic quantities as the chemical potentials of the various atomic species included in the modeling. However, a thermodynamic description cannot be compiled only from first-principles DFT calculations mainly due the immense computational work needed to treat finite temperature properties. A pragmatic approach to this problem is given in Papers I and IV, where we have made use of available thermodynamical data. The connection between DFT and thermodynamic modeling for the interfacial systems is described in Section 4.1.2.

The subsequent Section 4.2 present the modeling that we have applied in the appended papers to deal with solid/liquid and solid/solid interfaces. Obviously, the modeling does not capture the full thermodynamics of the complex systems studied and assumptions and simplifications will be pointed out.

## 4.1 Thermodynamics

### 4.1.1 Thermodynamics of interfaces

The most important property in a thermodynamic description of an interface is its interface energy  $\gamma$  [38]. To define  $\gamma$ , we consider a system of two phases which are in contact along a planar interface. The phases can be different (thus forming an interphase boundary), the same (intrapphase boundary) or one of them may be a vapour phase (surface). The phases and the dividing interface are held at constant temperature  $T$  and pressure  $P$  and are assumed to be in equilibrium with reservoirs at the same  $T$  and  $P$  providing atoms of component  $i$  at a chemical potential  $\mu_i$ . Furthermore, the two adjoining phases are assumed to be large in comparison with the interface system. As a consequence of a reversible change of the system, the total energy  $E$  will change according to [38]

$$dE = TdS - PdV + \sum_i \mu_i dN_i + \gamma dA, \quad (4.1)$$

where  $S$  is the entropy,  $V$  the volume of the interface system,  $N_i$  the number of atoms of component  $i$  and  $A$  the interfacial area. With the exception of the  $\gamma dA$  term, Eq. (4.1) is analogous to that of a bulk system. We here choose to consider  $dA$  as the change of area  $A$  as a result of adding atomic sites to the interface rather elastic stretching of the interface, since in this case interface energy and interface tension will be the same.

Several ways of defining  $\gamma$  as derivatives of thermodynamic potentials exist, e. g.  $\gamma = (\partial E / \partial A)_{S, V, N_i}$  [38]. For the applications in this Thesis, the most useful way of expressing  $\gamma$  is to relate it to Gibbs energy  $G$  defined by

$$G = E + PV - TS. \quad (4.2)$$

By integrating Eq. (4.1) into

$$E = TS - PV + \sum_i N_i \mu_i + \gamma A \quad (4.3)$$

and using Eq. (4.2) one finds that

$$\gamma = \frac{1}{A} \left( G - \sum_i N_i \mu_i \right). \quad (4.4)$$

Here, the quantity  $\sum_i N_i \mu_i$  can be identified with the Gibbs energy that  $N_i$  atoms of type  $i$  at chemical potential  $\mu_i$  would have if accumulated into separate bulk phases in the absence of the interface. Hence,  $\gamma$  is the excess Gibbs energy per unit interfacial area due to the presence of the interface.

Another important interfacial quantity is the work of adhesion  $W_{\text{adh}}$ , which is the change in free energy associated with the cleavage of the interface into two separate surfaces [113]. The separation is defined to occur along a reversible path on which

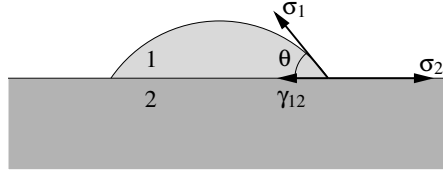


**Figure 4.1:** The quantities involved in the thermodynamic force balance for the droplet-substrate-vapor contact line.

the chemical potentials  $\mu_i$  of the atoms of all components in the separating structures are constant, i. e. the system is in chemical equilibrium during the separation. The work needed to separate the interface is then given by the Dupré equation

$$W_{\text{adh}} = \sigma_1 + \sigma_2 - \gamma_{12}, \quad (4.5)$$

where  $\sigma_1$  and  $\sigma_2$  are the surface energies (liquid-vapor or solid-vapor surfaces) and  $\gamma_{12}$  the interface energy of the adjoining phases.

Interface energies are very difficult to measure experimentally, but the work of adhesion between a liquid and a solid can be measured in sessile drop experiments. In these experiments, liquid is dropped onto a planar substrate to form a small droplet. By considering a thermodynamic force balance along the droplet (1) - substrate (2) - vapor contact line (see Figure 4.1), a relation between the interface energy  $\gamma_{12}$ , the surface energies  $\sigma_1$  and  $\sigma_2$ , and the contact angle  $\theta$  can be obtained, expressed by the Young equation as

$$\sigma_2 - \sigma_1 \cos \theta - \gamma_{12} = 0. \quad (4.6)$$

Combining Eqs. (4.5) and (4.6) yields the Young-Dupré equation

$$W_{\text{adh}} = \sigma_1 (1 + \cos \theta). \quad (4.7)$$

Extensive sessile drop experiments between liquid metals and carbides of interest in the cemented carbides system show that the wetting between Co and carbides formed with metals from group VI-B in the periodic system ( $\text{Cr}_3\text{C}_2$ ,  $\text{Mo}_2\text{C}$ , WC) is perfect ( $\theta = 0$ ) [114]. This implies that the work of adhesion between the metal and carbide reduces to  $W_{\text{adh}} = 2\sigma_{\text{Co}}$ , where  $\sigma_{\text{Co}}$  is the surface energy of Co. One can thus draw the conclusion, that a WC surface in chemical equilibrium with liquid Co will be completely covered by Co. Hence, even with known values of Co and carbide surface energies in the absence of Co, a sessile drop experiment cannot provide a definite value of the carbide/Co interface energy.

A conceptually simpler interfacial quantity is the ideal work of separation  $W_{\text{sep}}$ , which is defined as the reversible work needed to separate the interface into two free surfaces in a process where plastic and diffusional degrees of freedom are suppressed [113]. In a real cleavage experiment, the work needed to cleave an interface would necessarily be larger than  $W_{\text{sep}}$  due to dissipation arising mainly in the plastic processes accompanying the real cleavage.  $W_{\text{sep}}$  is a direct measure of the mechanical

strength of the interface, and can be written as a modification of Eq. (4.5) into

$$W_{\text{sep}} = \sigma'_1 + \sigma'_2 - \gamma_{12}, \quad (4.8)$$

where the primed surface energies  $\sigma'_1$  and  $\sigma'_2$  refer to unequilibrated surfaces. It should hold that  $W_{\text{sep}} \geq W_{\text{adh}}$ , since  $\sigma'_1 + \sigma'_2 \geq \sigma_1 + \sigma_2$ . Both  $W_{\text{adh}}$  and  $W_{\text{sep}}$  are thermodynamically sound quantities related to different reversible cleavage paths corresponding to fixed surface compositions or chemical potentials, respectively [115]. Disregarding irreversible processes, which of the quantities that best reflects the strength of an interface in a real application depends on the “speed” of the fracture. If the fracture is rapid compared to typical relaxation times for diffusion processes near the cleavage surfaces,  $W_{\text{sep}}$  will be the relevant measure of strength.

From a theoretical point of view,  $W_{\text{sep}}$  is more amenable to atomistic calculation than  $W_{\text{adh}}$ . The only problem in an atomistic calculation of  $W_{\text{sep}}$  for a given interface is to find the most low-energetic cleavage surface, whereas a calculation of  $W_{\text{adh}}$  requires a complete thermodynamic description of the interface and surfaces. A comparison of calculated  $W_{\text{sep}}$  and experimentally acquired  $W_{\text{adh}}$  by Ramqvist [114] for some of the interfaces treated in Paper II is given in Figure 4.2. A quantitative agreement is not seen and can obviously not be anticipated either. The calculated work of separation between the carbides and Co are seen to be scattered around  $5 \text{ J/m}^2$ , with the exception of the cubic MC(001)/Co interfaces which have consistently lower work of separation. The experimentally worse wetting of TiC could thus possibly be explained by the presence of stable TiC(001) surfaces in the carbide specimen.

Few estimations of carbide/Co interface energies based on experiment exist in literature. Warren related measured contiguities and average number of contacts between carbide grains in sintered materials to ratios between grain boundary and solid/liquid interface energies [116]. He estimated energies for the TiC/Co and TaC/Co interfaces to be around  $0.5 \text{ J/m}^2$ , but due to the complete Co wetting of WC he could only give a lower limit of the WC/Co interface energy of  $0.575 \text{ J/m}^2$ . Similar results were obtained by the same author using a simple thermodynamic model to predict carbide/liquid interfaces [117]. In WC-Co-TiC grades, full densification is harder to achieve than in straight WC-Co grades (see e. g. p. 154 in Ref. [3]) and often requires longer sintering times or higher temperatures, which has been explained by the poorer wetting of Co on TiC. This experimental behavior should in that case be reflected by the rather small difference in the measured work of adhesion between TiC/Co and WC/Co ( $\sim 0.2 \text{ J/m}^2$  from [114]), while one notes that estimated WC/Co and TiC/Co interface energies are more similar.

### 4.1.2 Connecting DFT and thermodynamics

DFT is a theory that accurately predicts total energies of isolated systems. It is however not obvious how to approximately calculate a quantity as interface energy which depends on free energy differences. Over the years, a strategy of combining *ab-initio* calculations with thermodynamic concepts has been worked out and applied to determine e. g. stabilities of oxide surfaces and oxide films of different

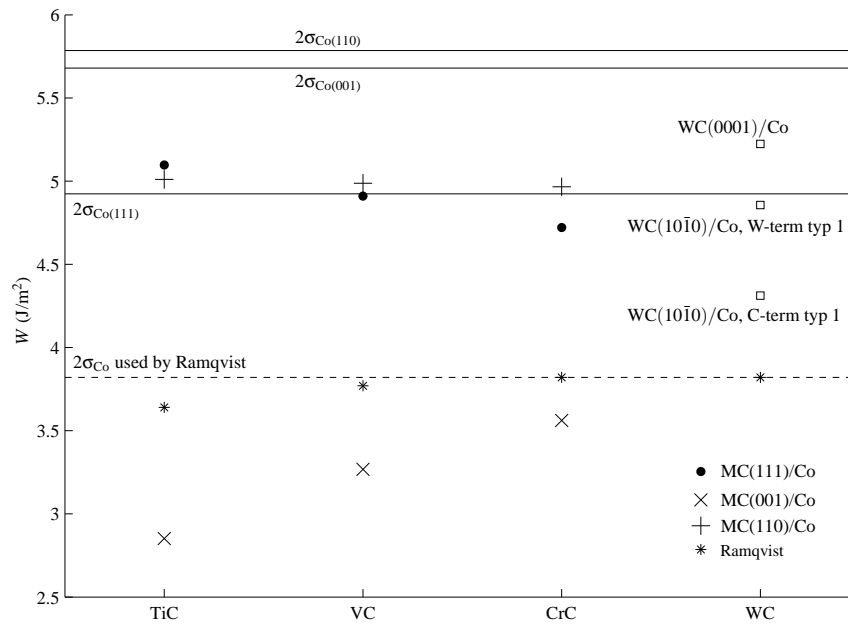


**Figure 4.2:** Work of separation for carbide/Co interfaces considered in Paper II. TiC, VC and CrC are modeled in the cubic carbide structure, and WC in its hexagonal structure. For the surfaces and interfaces of mixed metal-carbon termination (MC(001) and MC(110), where M = Ti, V or Cr) the ideal work of separation  $W_{\text{sep}}$  is presented. For the surfaces and interfaces of singular metal or carbon termination (MC(111), WC(0001) and WC(10 $\bar{1}$ 0)) the optimal termination with respect to energy is chosen separately for surface and interface, corresponding to a situation where C atoms may diffuse and are in equilibrium with graphite. The presented work of separation is thus in the range between  $W_{\text{sep}}$  and  $W_{\text{adh}}$ . The experimental values are taken from Ref. [114]. The experimental values for Cr corresponds to the Cr<sub>3</sub>C<sub>2</sub> phase. As reference, the work  $W = 2\sigma_{\text{Co}}$  needed to separate bulk Co into two surfaces of some different orientations is also presented.

stoichiometry under varying oxygen pressure [118, 119, 120]. The method used in these works can be carried over to the systems of interest in this thesis, and will be used in the account below for the W-C-Co system. The WC/Co interface will here be taken as an example, but the method and conclusions are applicable also to WC/WC grain boundaries and other MC/Co interfaces.

In the simulations of interface systems in this thesis, the Gibbs energy  $G$  of Eq. (4.2) is approximated by the total energy  $E$  obtained from DFT, i. e.

$$G \approx E. \quad (4.9)$$

This means that the interface energy of Eq. (4.4) in the WC-Co system is approximated as

$$\gamma = \frac{1}{A} (E - N_W \mu_W - N_C \mu_C - N_{Co} \mu_{Co}). \quad (4.10)$$

The bulk phases, WC and Co, in the vicinity of the interface are assumed to act as reservoirs for the interface system. Thus, in equilibrium it holds that  $\mu_W + \mu_C = G_{WC}$ , where  $G_{WC}$  is the Gibbs energy per formula unit of WC. We now approximate  $G_{WC}$  with the DFT total energy per formula unit  $E_{WC}$  and set

$$\mu_W + \mu_C = E_{WC} \quad (4.11)$$

and similarly for Co,

$$\mu_{Co} = E_{Co}, \quad (4.12)$$

where  $E_{Co}$  is the DFT total energy per Co atom in the Co bulk fcc structure. Both  $E_{WC}$  and  $E_{Co}$  are determined in separate supercell calculations of the respective bulk materials.

For systems with  $N_W = N_C$ , Eq. (4.11) is sufficient to determine the interface energy. However, in case  $N_W \neq N_C$ ,  $\mu_W$  or  $\mu_C$  needs to be determined separately. As described in Section 2.1.2, the WC+Co two-phase field borders to the three-phase fields WC+Co+ $\eta$  and WC+Co+graphite for low and high carbon content, respectively. It is therefore convenient to relate  $\mu_C$  to graphite rather than trying to relate  $\mu_W$ ,  $\mu_C$  and  $\mu_{Co}$  to the mixed (Co,W)<sub>6</sub>C  $\eta$ -phase. Within the two-phase field, it holds that  $\mu_C = G_{\text{graphite}} - \Delta\mu_C$ , where  $G_{\text{graphite}}$  is the Gibbs energy per atom of graphite and  $0 \leq \Delta\mu_C \lesssim 0.2 \text{ eV}$  with the lower (upper) limit of  $\Delta\mu_C$  in the graphite ( $\eta$ ) limit (see Section 2.1.2). Analogously to previous approximations, we set

$$\mu_C = E_{\text{graphite}} - \Delta\mu_C, \quad (4.13)$$

where  $E_{\text{graphite}}$  is the total energy per atom of graphite.

Technically,  $E_{\text{graphite}}$  is not directly obtained from a DFT calculation of carbon in the graphite structure. Instead, the total energy of diamond  $E_{\text{diamond}}$  is used and corrected with the assessed enthalpy difference at low temperature given by Ref. [121]. In literature, this procedure has been motivated by the fact that standard DFT in the LDA or GGA approximation does not accurately predict the structure of graphite due to the neglect of the non-local electron correlation responsible for the inter-layer

bonding between graphene sheets (see e. g. [26, 122]). In the context of obtaining a correct reference energy of carbon, a comparison of total energy differences between graphite and diamond for different functionals, the size of the van der Waals correction for graphite [123], and experimental enthalpy differences [121], also suggests that an error of the same magnitude comes from the PBE functional used in the appended papers, which predicts a too low energy for the graphene sheets making up graphite. This would be in line with PBE's supposed underestimation of energies for surface structures [95].

With all approximations defined, Eq. (4.10) turns into

$$\gamma = \frac{1}{A} (E - N_W E_{WC} - (N_C - N_W) E_{\text{graphite}} + (N_C - N_W) \Delta\mu_C - N_{Co} E_{Co}). \quad (4.14)$$

This equation is in many respects analogous to surface energy expressions of oxide surfaces in Ref. [119]. In that work, the oxygen potential is allowed to vary and a connection is made to the partial oxygen pressure by applying an ideal-gas model for the  $O_2$  atmosphere. In our case, such simple relation between carbon content and carbon potential does not exist, and one has to use thermodynamical databases to relate carbon content with  $\Delta\mu_C$ .

For transition metal additions  $M$  to the  $W-C-Co$  system and  $WC/Co$  interfaces, Eq. (4.14) is extended with the term  $-N_M \mu_M$  as done in Paper II. For metals of group IV and V present as cubic carbides in the alloy, the chemical potential of  $M$ ,  $\mu_M$ , is taken from the relation  $\mu_M = E_{\text{nacl } MC} - \mu_C$ , where  $E_{\text{nacl } MC}$  is the DFT total energy of  $\text{nacl } MC$ . This corresponds to an upper bound of  $\mu_M$  since the  $W$  and  $M$  atoms in the real material mix in the cubic  $(W,M)C_x$  phase.

The accuracy of Eq. (4.14) depends on to what degree errors from the  $G \approx E$  approximation cancel when summed. With certainty, the neglect of the  $PV$  term in  $G$  should not induce any noticeable error for typical pressures ( $P \lesssim 100 \text{ atm}$ ) and supercell sizes ( $V \lesssim 10^3 \text{ \AA}^3$ ) [119]. Leaving out  $PV$ , the remaining part of  $G$  equals the Helmholtz energy  $F$ . Most of the difference between  $F$  and  $E$  stems from atomic vibrations, and one can therefore decompose  $F$  into

$$F = E + F_{\text{vib}}, \quad (4.15)$$

where  $F_{\text{vib}}$  is the free energy due to vibrations which includes the zero-point vibration energy. It is often assumed that  $F_{\text{vib}}$  is small [119] and that temperature dependent terms in  $F_{\text{vib}}$  tend to cancel between condensed phases [124]. Considering Eq. (4.14) for  $N_C = N_W$ , the latter statement will hold exactly true if vibrational properties of all the  $W$  and  $C$  ( $Co$ ) atoms in the interface system equal those of bulk  $WC$  ( $Co$ ). Considering the case  $N_C > N_W$ , the statement will hold if also the excess carbon atoms vibrate as in graphite. The graphite structure is considerably more open than the  $WC/Co$  interface structure, and it is therefore instructive to also use the more hard-bonded diamond phase as a reference state for carbon. In such case, Eq. (4.14) would change into

$$\gamma = \frac{1}{A} (E - N_W E_{WC} - (N_C - N_W) E_{\text{diamond}} + (N_C - N_W) \Delta\mu_C^* - N_{Co} E_{Co}), \quad (4.16)$$

where  $\Delta\mu_C^*$  is defined by  $\mu_C = G_{\text{diamond}} - \Delta\mu_C^*$ . The difference between Eqs. (4.16) and (4.14) is  $\frac{1}{A}(N_C - N_W)((G_{\text{diamond}}(T) - G_{\text{graphite}}(T)) - (E_{\text{diamond}} - E_{\text{graphite}}))$ . For a complete C-terminated basal WC surface at sintering temperatures ( $T = 1410^\circ\text{C}$ ) this corresponds to an increase in  $\gamma$  of around  $0.15\text{J/m}^2$  (using energy expressions from Ref. [121]) compared with Eq. (4.14). For  $N_W > N_C$ , a similar calculation relating  $\mu_W$  to fcc W as a reference state would give a decrease in  $\gamma$  of around  $0.14\text{J/m}^2$  (using energy expressions from Refs. [125, 121, 126]) compared with Eq. (4.14). These values may serve as examples of the magnitude of the error induced by the  $G \approx E$  approximation at finite temperatures.

Reuter *et al* calculated the vibrational contribution to an oxide surface energy assuming an Einstein model, in which vibrational frequencies of the atoms in the outmost surface layer was allowed to vary with respect to corresponding characteristic bulk frequencies [119, 127]. Following this procedure for the WC/Co interface with a characteristic vibration frequency of 20 THz from the optical branch of the WC phonon spectrum [128] set to vary  $\pm 30\%$  at the interface would give a change in  $\gamma$  of maximally around  $\pm 0.3\text{J/m}^2$  in the temperature range of interest. Thus, vibrational effects at the interface make a substantial contribution to the absolute value of the interface energy.

It must here be pointed out, that the discussion above assumes that the interface has a well-defined structure, meaning that each atom has a mean position around which it vibrates. At high-temperatures, the WC/Co interface is a solid/liquid interface where temperature-dependent contributions to the interface energy are dominated by differences in configuration free energies between the liquid and the interface layer. However, it is likely that relative differences between energies for different carbide/Co interfaces of similar structure are less affected, and this assumption is used in Paper I and II.

To determine the effect of temperature on  $\gamma$  in a more exact manner, an explicit treatment of temperature is needed. This could involve molecular dynamics simulations or, more feasibly, phonon calculations in the density functional perturbation theory (DFPT) scheme [129]. The latter would produce the correct temperature dependence of interface energies to the extent that the vibrational free energy can be calculated in the quasi-harmonic approximation. Thus, DFPT would be applicable for carbide grain boundaries and carbide surfaces, although not for the carbide/metal interface in which the metal phase is close to or above its melting temperature.

### 4.1.3 Solubility

Motivated by atom-probe measurements of WC grains in doped WC-Co, we studied the solubility of various transition metals in WC in Paper IV. To model the mixing and solubility of components  $i$ , a Gibbs energy  $G_f$  per formula unit of the mixed phase is needed. The simplest starting point is the ideal solution model, in which

$$G_f = \sum_i x_i G_i + k_B T \sum_i x_i \ln x_i, \quad (4.17)$$

where  $k_B$  is Boltzmann's constant and  $G_i$  is the Gibbs energy per formula unit of the phase containing only  $i$ .  $x_i$  is the fraction of  $i$ , i. e.  $x_i = N_i/N$  where  $N_i$  is the number of  $i$  atoms and  $N$  the total number of atoms (or, more generally, constituents). For a solid, this would correspond to the fraction of atomic sites occupied by  $i$ . The first term of Eq. (4.17) represents the Gibbs energy of a mechanical mixture of the  $i$ , and the second term is the ideal mixing entropy  $S^{\text{mix}}$  per formula unit derived by considering the number of distinguishable arrangements and using Boltzmann's expression  $S^{\text{mix}} = \frac{k_B}{N} \ln((\sum_i N_i)! / \prod_i N_i!)$  and Stirling's formula as done in any standard text on thermodynamics (e. g. [130]).

To approach a realistic description of an alloy, the interaction between different components must be taken into account, by adding an excess Gibbs energy per formula unit term  $G^{\text{xs}}$  to Eq. (4.17). In its simplest form, the regular solution model,  $G^{\text{xs}}$  takes the form

$$G^{\text{xs}} = \sum_i \sum_{j>i} x_i x_j L_{ij}, \quad (4.18)$$

where  $L_{ij}$  is a binary interaction parameter between components  $i$  and  $j$ . Such a model is consistent with a mean-field treatment of an alloy in which the energy is given as a sum of pairwise contributions  $E_{ij}$  from pairs of atom types  $i$  and  $j$ . Defining an energy difference for the different bonds,  $\varepsilon_{ij} = E_{ij} - \frac{1}{2}(E_{ii} + E_{jj})$ , the mean-field approach gives  $L_{ij} = \frac{z}{2}\varepsilon_{ij}$ , where  $z$  is the number of bonds per atom [130, 4]. Though a physical meaning of  $L_{ij}$  can be understood from this comparison, it is in thermodynamic modeling often treated as an adjustable temperature-dependent parameter and its physical origin – be it electronic, vibrational, configurational or a combination thereof – need not be clear.

The  $L_{ij}$  can be further expanded into a Redlich-Kister polynomial  $L_{ij} = \sum_m (x_i - x_j)^m \cdot {}^m L_{ij}$  or other composition-dependent forms [4]. For ternary systems, corresponding ternary interaction contributions  $\sum_{i,j>i,k>j} x_i x_j x_k L_{ijk}$  and expansions thereof may be added. For alloys with pronounced order, long-range or short-range, the mixing entropy contained in Eq. (4.17) will not be a good description of the configurational entropy. Such systems are better treated with e. g. cluster expansion models [131, 4] in which the energy is expanded into contributions from small atomic clusters. Instead of further elaborating on alloy modeling, which is out of scope for this text, we conclude that the regular solution model is fully sufficient to deal with the low concentrations found of transition metal solubilities in WC in Paper IV. In fact, the calculated concentrations are so small that they could have been treated as simple thermal defects.

Starting from the relation

$$\mu_i = \left( \frac{\partial}{\partial N_i} (NG_f) \right)_{T, N_{j \neq i}}, \quad (4.19)$$

the regular solution model gives a simple equation for the chemical potential  $\mu_i$ . Assuming for brevity a binary mixture ( $i = 1, 2$ ,  $L_{12} = L$ ), the potential for component 1 reduces to [4]

$$\mu_1 = G_1 + k_B T \ln x_1 + (1 - x_1)^2 L. \quad (4.20)$$

For a mixed (W,M)C (M=Ti, V, etc.) phase as modeled in Paper IV, which consists of both a metal and a carbon sublattice, this equation is not directly applicable. The metal atoms are assumed to mix only on the metal sublattice, and the addition of one metallic atom as prescribed by Eq. (4.19) necessarily involves the addition of also one carbon atom. Thus Eq. (4.20) needs to be slightly altered with an addition of the carbon potential  $\mu_C$  to its left hand side (see Paper IV).

As for the interfacial systems, the Gibbs energies appearing in the expressions were approximated by total energies in Paper IV. Since theories for solubility are readily available, improvements (e. g. inclusion of vibrational free energy) of this simple approach are obvious. In this work, they were not pursued.

## 4.2 Interface modeling

In Section 4.1.1, the interface energy  $\gamma$  was defined in Eq. (4.4). Although already a strong approximation, the direct application of Eq. (4.14) for an arbitrary interface is still beyond the capabilities of today's first-principles modeling. A real interface can be sharp or diffuse, planar or non-planar, reconstructed, contain segregants, precipitates, vacancies or dislocations, etc. Incorporation of some of these effects into an atomistic model are possible, but a fully realistic description of an interface remains intractable. To reach a computationally feasible model of an interface, several simplifications have to be made. In this section, we present and discuss the modeling of interfaces used in the appended papers. The choices done in the atomistic modeling are guided and motivated by the experimental investigations reviewed in Chapter 2.

In a multiphase material, two different types of interfaces are present: intra- and interphase boundaries. The former category includes grain boundaries and stacking faults, whereas the latter include the interfaces between different phases. The papers in this thesis deal with interphase boundaries between metal and ceramic. The properties of an interface depend strongly on its atomic structure and this is certainly true also for the interface energy. As a necessary input for first-principles modeling, a reasonable geometric setup of atoms in the interface system is a crucial input of all computational interfacial studies. Thus, this section begins with reviewing some basic concepts of geometry in crystal/crystal interfaces.

### Geometry of an interface

Macroscopically, an interface between two crystals has five degrees of freedom [38]. The *orientation relationship* describes the relative rotation between two crystals and provides three degrees of freedom. These are usually specified by a common rotation vector (two degrees of freedom) and a common vector perpendicular to the rotation vector (one degree of freedom). These first three degrees of freedom completely specify the relation between the lattices of the adjoining crystals. Two more degrees of freedom are necessary to specify also the interface plane, which can be done by giving the direction of the interface normal with respect to the common rotation vector between the crystals.

With these five degrees of freedom specified, all geometric thermodynamic variables are set [38] and a full atomic structure of the interface could, in principle, be reconstructed from theoretical modeling by minimizing a grand potential of the interfacial system in contact with reservoirs of well-defined chemical potentials. In fact, only the three degrees of freedom relating the lattice orientations would be needed in such hypothetical simulation, and may be seen as boundary conditions fulfilled by the lattices far from the interface. The interface plane would then come out as a result when minimizing the grand potential of the system. A real example of this is the straightening of general  $\Sigma 2$  grain boundaries between WC grains into twist boundaries which occurs during sintering [37].

### Experimental input

In the current modeling, apart from defining the orientation relationship and interface orientation, further specification of the microscopic structure must be made. To this end, input from experimental investigations is very valuable. In the WC-Co system, WC grains are mostly bounded by  $\{0001\}$  and  $\{10\bar{1}0\}$  surfaces. Furthermore, high resolution electron microscopy imaging shows the WC/Co interfaces to be locally planar and atomistically sharp (in undoped WC-Co). This simplifies the atomistic modeling, as only various terminations of (W, C, or mixed) of the WC phase need to be considered. The sharpness of the interface region is in itself a motivation for an atomistic treatment of the interface, as it cannot be described as a continuous mixture of the WC and binder phase.

There is no preferential relation between the Co and WC in liquid phase sintered WC-Co, which can be explained by the large grain size of Co. During cooling from the liquid phase, Co nucleates at few places and as solidification proceeds, the growing Co grain will have no particular relation to the WC skeleton. Generally, the orientation between WC and Co is therefore completely random. Similarly, during the actual liquid phase sintering when the metal is in its melt state, there will be no long-range order in the WC/Co interface structure. WC-Co structures formed during solid state sintering may however contain Co areas with preferential orientation to the WC grains having well-defined orientation relationships [52], as do the Fe/VN interface modeled in Paper V and VI.

### The $\gamma$ -surface

The modeling of on one hand general WC/Co interfaces without any preferred orientation, and on the other hand, special structurally well-defined interfaces requires two different approaches to modeling. For both approaches, the  $\gamma$ -surface [38] is an essential theoretical tool. To define the  $\gamma$ -surface, we first consider the rigid body displacement of two grains joined at a planar, sharp interface. The displacement vector  $\vec{t}$  (defined with some origin in the interface) can be decomposed into a translation  $\vec{T}$  parallel to the interface and an interface separation  $\vec{d}$  normal to the interface. If there is a translational symmetry in the interface, a cell of non-identical displacements (CNID) may be defined.

The  $\gamma$ -surface is defined as the interface energy  $\gamma$  (defined by Eq. (4.4)) as a function of  $\vec{r} = \vec{T} + \vec{d}$ . For the  $\vec{T}$ -dependent coordinates,  $\gamma(\vec{T}, \vec{d})$  will have the periodicity of the CNID. With decreasing size of the CNID corresponding to a longer periodicity of the interface,  $\gamma(\vec{T})$  flattens out, and for a completely incommensurate interface lacking any periodicity thus having an empty CNID, the variations of  $\gamma(\vec{T})$  are zero.

### Misfit

An important topic of this thesis is to derive estimations of interface energies for various type of interfacial structures. An important concept is therefore the *coherence* of the interface. A measure of coherence valid for planar, sharp solid/solid interfaces is the misfit  $f$  which, assuming two crystal lattice parameters  $a^{(1)}$  and  $a^{(2)}$  ( $a^{(1)} > a^{(2)}$ ) in the interface plane, can be defined as

$$f = \frac{a^{(1)} - a^{(2)}}{\frac{1}{2}(a^{(1)} + a^{(2)})}. \quad (4.21)$$

Depending on the value of  $f$ , the interfaces are divided into three groups: Coherent, semicoherent and incoherent.

The *coherent* interface has zero misfit ( $f = 0$ ) and the lattices of the adjoining crystals match perfectly at the interface. In reality, coherent interfaces between dissimilar materials are rarely seen, but if the thickness of one of the (or both) phases is finite, the thinner phase can be strained to coherence, as may be the case for a thin film strained to a substrate. A coherent interface can also be the result of stand-off dislocations that accomodate the misfit not at the interface itself, but in the bulk phase. In some rare cases, (almost) coherent interfaces can form between solids of the same constituents but different Bravais lattices, such as fcc-Co and hcp-Co in the  $(111)_{\text{fcc}} \parallel (0001)_{\text{hcp}}$  interface.

A *semicoherent* interface has a small misfit,  $0 < f \lesssim 0.2$ . By considering a film growing on a substrate, it is apparent that for some thickness, it is energetically favorable to relieve the coherency strain and instead let the misfit be taken up by misfit dislocations. The name misfit dislocation could be misleading, since these dislocations are not defects, but a consequence of the geometry of the interface. If the interaction across the interface is pronounced enough to produce localized misfit dislocations, the interface will be characterized by large regions of good fit between the crystals (the coherent region) and small areas in the vicinity of the misfit dislocations, where the atomic structure is distorted.

An *incoherent* interface is the result of a large misfit  $f \gtrsim 0.2$  and/or weak bonding across the interface. Assuming an artificially increasing misfit, misfit dislocations will approach each other as  $f$  increases, and eventually the atomic displacements due to neighboring dislocations will cancel. An incoherent interface can also come from joining two crystals with differing surface lattice in the interface plane, such as a high-angle grain boundary. Incoherent interfaces do not show the long-range correlation in atomic displacement as semicoherent interfaces do.

Both practically and theoretically, it is very useful to determine the  $\gamma$ -surface defined above, but under the assumption that the semi- or incoherent interface is rendered coherent by an artificial compression (expansion) of the corresponding phases which yields a common interface lattice parameter  $a$ . For supercell calculations, this is necessary since the interface must be commensurate to fit within a supercell of finite size. Thus,  $\gamma(\vec{t})$  is calculated as

$$\gamma(\vec{t}) = \frac{1}{A} \left( E(\vec{t}) - \sum_i N_i \mu_i \right), \quad (4.22)$$

where  $E(\vec{t})$  is the energy of the artificially coherent interface system translated by  $\vec{t}$ ,  $N_i$  is the number of constituent  $i$  in the interface system, and  $\mu_i$  is the energy per atom  $i$  retrieved from a bulk calculation of the respective compressed (expanded) phases. This procedure excludes any direct elastic contributions to  $\gamma(\vec{t})$ . The choice of  $a$  in the interval  $a^{(2)} \leq a \leq a^{(1)}$  is somewhat arbitrary, but an appropriate method is to choose  $a$  so that the sum of elastic energy in both bulk phases is minimized and allow for a corresponding Poisson relaxation in directions along the interface normal. For the rather incoherent WC/Co interfaces studied here ( $f \approx 0.15$ ), this implies that practically all distortion will be in the soft Co phase.

For the coherent interface, the true interface energy  $\gamma$  is simply the minimum of the  $\gamma$ -surface,

$$\gamma_{\min} = \min_{\vec{t}} \gamma(\vec{t}). \quad (4.23)$$

For an incoherent interface of infinite dimension, the  $\gamma(\vec{t})$ -surface is reduced to a value independent of the in-plane translation  $\vec{T}$  (still dependent on  $\vec{d}$ ). We effectively take this constant value as the mean of the  $\gamma$ -surface defined according to

$$\gamma_{\text{mean}} = \int_A dA \min_{\vec{d}} \left[ \gamma(\vec{T}, \vec{d}) \right], \quad (4.24)$$

where  $A$  is the area of the surface cell. The integral should be interpreted as a mean value over local interaction configurations with properly assigned weights according to the symmetry of the point  $\vec{T}$  in the surface cell.

In Ref. [132], Christensen *et al* introduce a coherence parameter  $\alpha$  defined by

$$\gamma = \gamma_{\min} + \alpha(\gamma_{\text{mean}} - \gamma_{\min}), \quad (4.25)$$

where  $\alpha = 0$  corresponds to the perfectly coherent structure and  $\alpha = 1$  to the completely incoherent structure. The true value of  $\gamma$  should lie somewhere between these values (or possibly above if  $\gamma(\vec{t}, \vec{d})$  depends strongly on the interface separation  $\vec{d}$ ).

### Semicoherent interfaces

For a semicoherent interface, the interface energy will lie somewhere between the coherent ( $\alpha = 0$ ) and incoherent ( $\alpha = 1$ ) limits, and the exact value of  $\alpha$  depends on the energy for creating misfit dislocations. Making a quantitative determination

of the interface energy in the semicoherent interface requires a model of the elastic response of the adjoining crystals. Such a model is developed in Paper V and VI, where we use the simple Peierls-Nabarro model of dislocations [133, 134] to determine the elastic energy of the semicoherent interface. The model assumes that the total interface energy  $\gamma$  may be decomposed into

$$\gamma = \gamma_{\text{el}} + \gamma_{\text{chem}}, \quad (4.26)$$

where  $\gamma_{\text{el}}$  is an elastic energy due to a periodic array of misfit dislocations derived from elasticity theory, and  $\gamma_{\text{chem}}$  is the chemical energy due to the presence of the interface.

For simplicity, assuming a one-dimensional misfit an analytic expression for the elastic energy  $\gamma_{\text{el}}$  as functional of the relative (atomic) displacements  $u(x)$  at the interface between two semifinite crystals can be derived

$$\gamma_{\text{el}}[u(x)] = -\frac{K_e}{4\pi p} \int_{-p/2}^{p/2} \int_{-p/2}^{p/2} \ln \left| \sin \frac{\pi}{p}(x-x') \right| \frac{\partial u(x')}{\partial x'} \frac{\partial u(x)}{\partial x} dx' dx, \quad (4.27)$$

where  $p$  is the periodicity of the interface ( $p = a^{(1)}a^{(2)}/(a^{(1)} - a^{(2)})$ ), and  $K_e$  is an energy factor for the interfacial misfit dislocation which depends on the elastic constants of the interfacing media (see Section 3.3 and Paper VI). The chemical energy is an integral of the  $\gamma$ -surface,

$$\gamma_{\text{chem}}[u(x)] = \frac{1}{p} \int_{-p/2}^{p/2} \gamma[U(x)] dx, \quad (4.28)$$

where  $U(x)$  is a disregistry across the interface (see Paper VI). Thus, appropriate weights to different parts of the  $\gamma$ -surface i. e. different translation states, are explicitly given by this integral by optimizing Eq. (4.26).

In Paper V, we show that this model accurately describes the interface energy of semicoherent interfaces by comparing with atomistic calculations using an EAM potential for Fe in the Fe/VN interface. We develop the model further in Paper VI, where we account for slabs of finite thickness and a two-dimensional periodic array of misfit dislocations. No simple analytical expressions exist for these more general cases, and hence finite-element calculations are used for the elastic response. To conclude, connecting to Eq. (4.25), it is for semicoherent interfaces of well-defined geometry possible to explicitly find the appropriate value of  $\alpha$ .

### Incoherent interfaces

We now turn to the more complex incoherent interfaces. For WC/Co interfaces, generally no assumptions of regular, well-ordered atomic structures can be made. In Ref. [26], Christensen *et al* calculate several local configurations of Co coherently placed on WC $\{10\bar{1}0\}$  surfaces, and shows through a Wulff construction that  $\alpha = 1$  predicts correctly – within the experimental error bound – the experimentally measured truncation of the prismatic surfaces of WC grains sintered in Co. As argued

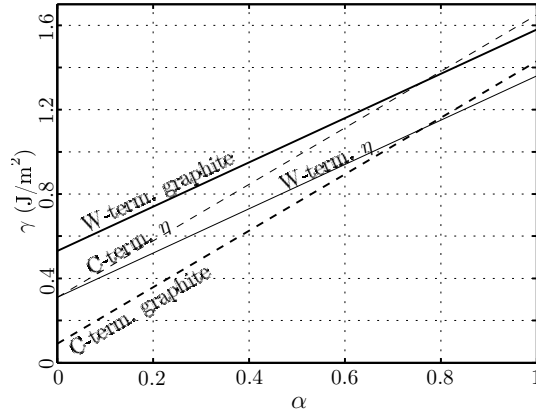


**Figure 4.3:** The interface energy  $\gamma$  as function of  $\alpha$  for the WC(0001)/Co(0001) interface.

in Ref. [26],  $\alpha = 1$  should be an appropriate approximation for the interface energy during liquid phase sintering. Then, Co atoms move over the WC surface constantly changing the atomic structure. Thus, relevant differences in interface energy between similarly structured WC/Co interfaces can be obtained from the differences of average values of ensembles of interfacial structures as given by Eq. (4.24).

The relevance of using an average value of the  $\gamma$ -surface to approximate the incoherent interface energy can to some extent be tested. In Paper III, we study several different WC(0001)/Co interfaces with varying W and C-termination. The systems are all fully relaxed corresponding to a  $T = 0\text{K}$  situation. At higher temperatures, the total energy of the interface system should increase with respect to these low-temperature values, as atoms begin to move over minima and maxima in the  $\gamma$ -surface.

$\gamma$  as a function of  $\alpha$  determined in coherent WC(0001)/Co(0001)<sub>hcp</sub> interfaces of W- and C-termination is given in Figure 4.3. Comparing with the results from Paper III, we see that for the W-terminated interface, low-energetic configurations (A, C, D, F) correspond to  $\alpha \approx 0.6$ . A more constrained configuration (B) and open-structured (E) correspond to  $\alpha \approx 1$ . Though, for C-terminated interfaces the assumption underlying Eq. (4.25) breaks down. The energy of C-Co bonds depend more strongly on both translation  $\vec{T}$  and interphase separation  $\vec{d}$  of the WC/Co interface as indicated by a more corrugated  $\gamma$ -surface in this case. The minimization implied by Eq. (4.24) will hence be associated with elastic energy. However, removing some low coordinated C atoms allowing for W-Co bonds to form instead, the interface energy drops, and the more low-energetic mixed W/C-terminated interface configurations correspond to  $\alpha \approx 0.4$  to 0.7.

To conclude, relaxed WC/Co interfaces are associated with  $\alpha$  from 0.4 to 0.7. More open or disordered structures would have  $\alpha \approx 1$ . We assume that  $\alpha = 1$  is the most appropriate choice for modeling a general, random interface especially for high-temperature conditions, where long-range order in the interface region is not expected. This pragmatic approach to interface modeling is used in Papers I and II. A more detailed treatment of interfacial relaxations as done in Paper III requires

large supercells and to probe the interfacial energetics as function of temperature, molecular dynamics simulations would be required. However, this would have made the study in Paper II an arduous task.

It should be stressed that only relevant interface energy *differences* are necessary for the conclusions made in Paper I and II. Our calculated values of interfacial energies only (approximately) include total energy effects to the true interface energy as defined in Eq. (4.4), which depends on free energy differences between interface and bulk systems. Structural disturbances lead to finite interface energies also between a solid and its corresponding liquid [135]. Such effects should to a large degree cancel when comparing interface energies of structures with similar interfacial geometry, but could be important when comparing interface energies between basal and prismatic WC/Co interfaces.

## Conclusions

### 5.1 Summary

This section provides a brief summary of the key results of the introductory discussion and appended papers. For details and complete references, the reader is referred to the individual papers and preceding chapters.

- We apply density functional theory to calculate interface energetics of metal-ceramic interfaces. To make predictions for general interfaces of random orientation, ensembles of local coherent interface configurations (an average of the  $\gamma$ -surface) are used. A justification for this pragmatic approach to interfacial modeling is provided by the results of Paper III.
- In Paper I, the method is applied to thin films of cubic VC in basal WC/Co interfaces. We find that V-rich films with a thickness of two atomic layers can be stabilized by interfacial effects, even when the corresponding bulk VC phase is unstable. This supports the idea that VC films are present in WC/Co interfaces and hinder WC grain growth also at high temperatures.
- In Paper II, we extend the analysis to examine the propensity for formation of films of cubic TiC, VC, CrC, ZrC, NbC, MoC, HfC, TaC and WC in the basal and prismatic interfaces between WC and Co. In order of decreasing propensity, VC, MoC, TiC and CrC are predicted to form films in the basal WC/Co interface, and MoC, VC and CrC films in the prismatic WC/Co interface. A comparison between the stability of VC films and those of other carbides provides a consistent explanation for the effectiveness of VC as grain growth inhibitor.
- In Paper IV, we study the solubility of transition metals in hexagonal WC with both atom-probe tomography and theoretical methods. Experimental

solubilities of Ta, Nb, Cr and V are in the  $10^{-3}$  range, Ti around  $10^{-5}$ , and solubilities of Zr and Co are below the detection limit. The agreement with theoretical predictions is satisfactory. The measured solubilities of Ta, Nb, Cr and V are higher than previously anticipated. From theoretical calculations, Cr is expected to have the highest possible solubility of the considered metals.

- In Paper V and VI, we extend the interfacial modeling to explicitly include the effect of misfit dislocations in semicoherent interfaces. We show that elastic energies can dominate the interfacial energetics of such interfaces. The method is applied to the low misfit (2%) Fe/VN interface and the predicted interfacial structure agrees with HREM imaging.

## 5.2 Outlook

In Papers I and II, an extensive set of DFT calculations has been used to calculate energetics of WC/Co interfaces with and without films of dopants. The theoretical results have clearly shown the effect of VC on interface energetics, but theoretical results for other dopants are less conclusive. From reviewing the literature on microstructural effects of the various additions, a similar picture is obtained. Notably, reported effects of especially Cr and Ti vary in literature. From the results of Paper II, these are the additives for which thin film configurations in WC/Co interfaces are on the limit of stability, and microstructural effects of these additives can therefore be expected to vary more sensitively on local and temporal variations of the Cr and Ti chemical potentials throughout a sintering cycle.

The structural changes of WC/Co basal and prismatic interfaces induced by doping have been well characterized by HREM imaging during the last decades. Films of cubic structure have been imaged in Ti-, V- and Cr-containing WC-Co, but estimations of the segregated amount of additive in WC/Co interfaces vary. Except for reports on some other interface structures in VC-Cr<sub>3</sub>C<sub>2</sub> co-doped material [71], the presence of cubic structures in WC/Co interfaces in doped material is therefore well established although the exact composition at the interface is still unknown. In Paper I, it was rather implicitly assumed that the composition of the film should be similar to that of bulk (V,W)C. To determine composition in an accurate manner, further modeling can be considered.

Due to the systematic treatment of interface structures in Paper II, only a rather small set of DFT calculations for films of mixed composition would need to be added to the thousands of simulated interfacial configurations underlying Paper II in order to fit a multilayer segregation model extending upon e. g. the one of Guttman [136]. With proper treatment of interfacial thermodynamics [137], a segregation model based on parameters derived from DFT would be a sound starting point for further quantitative modeling of WC/Co interfaces. Such modeling need not be based solely on first-principles and judging from the success of CALPHAD-type modeling of bulk phases, it should not. A combination of input from DFT calculations – such as the ones presented in this thesis – and from accurate experimental data – such as the

ones from a recent atom-probe tomography investigation of WC/Co interfaces [138] – is probably the best way to obtain a predictive and quantitative model of interface structures and energetics. Knowing the composition at interfaces as function of doping and temperature would clearly be of technological use.



# Acknowledgments

Firstly, I would like to thank Göran Wahnström for being a supportive and patient supervisor and for the guidance provided throughout this project.

Secondly, I would like to thank all participants of this research project: Jonathan Weidow and Hans-Olof Andrén of Chalmers; Susanne Norgren *et al* of Sandvik; Bo Jansson and Jenni Zackrisson *et al* of Seco Tools; Sabine Lay, Valérie Bounhoure and Jean-Michel Missiaen of INPGrenoble. Several more people have been part of the project at some time. They are included in the *et al* and not forgotten. I would particularly like to thank everyone participating in the project meetings. I have learnt a lot during these meetings and they have been most valuable for my understanding of materials in general and cemented carbides in particular.

Past and present members of the Material and Surface Theory group are also acknowledged for help and fruitful discussions.



# Bibliography

- [1] H. Pastor, in *Proceedings of the 1996 European Conference on Advances in Hard Materials Production* (, Stockholm, Sweden, 1996), p. 3.
- [2] E. Lassner and W.-D. Schubert, *Tungsten - Properties, Chemistry, Technology of the Element, Alloys, and Chemical Compounds* (Kluwer Academic / Plenum Publishers, New York, 1999).
- [3] G. S. Upadhyaya, *Cemented tungsten carbides - Production, properties, and testing* (Noyes Publications, Westwood, New Jersey, 1998).
- [4] H. L. Lukas, S. G. Fries, and B. Sundman, *Computational thermodynamics - The Calphad method* (Cambridge University Press, Cambridge, United Kingdom, 2007).
- [5] S. Dudy, *Microscopic theory of wetting and adhesion in metal-carbonitride systems*, Ph.D. thesis, Chalmers University of Technology, Göteborg University, Göteborg, 2002.
- [6] M. Christensen, *Strength and stability of interfaces in cemented carbides*, Ph.D. thesis, Chalmers University of Technology, Göteborg University, Göteborg, 2004.
- [7] B. Aronsson, *The origins and growth of cemented carbides* (Sandvik Group, Stockholm, 2005).
- [8] J. Gurland, *New scientific approaches to development of tool materials*, Int. Mater. Rev. **33**, 151 (1988).
- [9] W. D. Schubert, A. Bock, and B. Lux, *General aspects and limits of conventional ultrafine WC powder manufacture and hard metal production*, Int. J. Refract. Met. Hard Mater. **13**, 281 (1995).
- [10] Z. Z. Fang, X. Wang, T. Ryu, K. S. Hwang, and H. Y. Sohn, *Synthesis, sintering, and mechanical properties of nanocrystalline cemented tungsten carbide - a review*, Int. J. Refract. Met. Hard Mater. **27**, 288 (2009).

- [11] K. Christoffel, in *Proceedings of the 17th International Plansee Seminar, vol. 3*, edited by L. S. Sigl, P. Rödhammer, and H. Wildner (Plansee Group, Reutte, Tyrol, Austria, 2009), p. PL7.
- [12] J. W. Lee, D. Jaffrey, and J. D. Browne, *Influence of process variables on sintering of WC-25 wt-%Co*, Powder Metall. **23**, 57 (1980).
- [13] B. Aronsson, *Processing-properties relationship in cemented carbide*, Key Eng. Mater. **29-31**, 529 (1989).
- [14] H. E. Exner, *Physical and chemical nature of cemented carbides*, Int. Met. Rev. **24**, 149 (1979).
- [15] P. Ettmayer, *Hardmetals and cermets*, Annu. Rev. Mater. Sci. **19**, 145 (1989).
- [16] B. Meredith and D. R. Milner, *Densification mechanisms in the tungsten carbide-cobalt system*, Powder Metall. **19**, 38 (1976).
- [17] C. H. Allibert, *Sintering features of cemented carbides WC-Co processed from fine powders*, Int. J. Refract. Met. Hard Mater. **19**, 53 (2001).
- [18] G. Gille, B. Szesny, K. Dreyer, H. van den Berg, J. Schmidt, T. Gestrich, and G. Leitner, *Submicron and ultrafine grained hardmetals for microdrills and metal cutting inserts*, Int. J. Refract. Met. Hard Mater. **20**, 3 (2001).
- [19] Z. Fang, P. Maheshwari, X. Wang, H. Y. Sohn, A. Griffo, and R. Riley, *An experimental study of the sintering of nanocrystalline WC-Co powders*, Int. J. Refract. Met. Hard Mater. **23**, 249 (2005).
- [20] S. Haglund and J. Ågren, *W content in Co binder during sintering of WC-Co*, Acta Mater. **46**, 2801 (1998).
- [21] M. Göthelid, S. Haglund, and J. Ågren, *Influence of O and Co on the early stages of sintering of WC-Co: A surface study by AES and STM*, Acta Mater. **48**, 4357 (2000).
- [22] J.-M. Missiaen, *Solid-state spreading and sintering of multiphase materials*, Mater. Sci. Eng., A **475**, 2 (2008).
- [23] J. Gurland, *Current views on the structure and properties of cemented carbides*, Jernkont. Ann. **147**, 6 (1963).
- [24] K. Frisk and A. Markström, *Effect of Cr and V on phase equilibria in Co-WC based hardmetals*, Int. J. Mater. Res. **99**, 287 (2008).
- [25] A. Markström, B. Sundman, and K. Frisk, *A revised thermodynamic description of the Co-W-C system*, J. Phase Equilib. Diff. **26**, 152 (2005).

- [26] M. Christensen, G. Wahnström, C. Allibert, and S. Lay, *Quantitative analysis of WC grain shape in sintered WC-Co cemented carbides*, Phys. Rev. Lett. **94**, 066105 (2005).
- [27] P. Gustafson, *A thermodynamic evaluation of the C-Mo-W system*, Z. Metallkd. **79**, 397 (1988).
- [28] M. Brieseck, M. Bohn, and W. Lengauer, in *Proceedings of the 17th International Plansee Seminar, vol. 2*, edited by L. S. Sigl, P. Rödhammer, and H. Wildner (Plansee Group, Reutte, Tyrol, Austria, 2009), p. HM45.
- [29] Z. Tükör, W. D. Schubert, A. Bicherl, A. Bock, and B. Zeiler, in *Proceedings of the 17th International Plansee Seminar, vol. 4*, edited by L. S. Sigl, P. Rödhammer, and H. Wildner (Plansee Group, Reutte, Tyrol, Austria, 2009), p. HM44.
- [30] H.-O. Andrén, *Microstructures of cemented carbides*, Mater. Des. **22**, 491 (2001).
- [31] A. Fernández Guillermet, *Critical evaluation of the thermodynamic properties of cobalt*, Int. J. Thermophys. **8**, 481 (1987).
- [32] J. Weidow, S. Norgren, and H.-O. Andrén, *Effect of V, Cr and Mn additions on the microstructure of WC-Co*, Int. J. Refract. Met. Hard Mater. **27**, 817 (2009).
- [33] G. Wirmark and G. L. Dunlop, in *Proceedings of the International Conference on the Science of Hard Materials, held August 23-28 1981 in Jackson, Wyoming* (Plenum Press, New York, U.S.A., 1983), p. 311.
- [34] A. Fernández Guillermet, *Composition dependence of the Curie temperature of Co-W-C alloys predicted from thermodynamic data*, Z. Metallkd. **80**, 549 (1989).
- [35] A. Jaroenworarluck, T. Yamamoto, Y. Ikuhara, T. Sakuma, T. Taniuchi, K. Okada, and T. Tanase, *Interface and grain boundary structure in WC-Co*, Ceram. Trans. **99**, 501 (1998).
- [36] Y. Wang, M. Heusch, S. Lay, and C. H. Allibert, *Microstructure evolution in the cemented carbides WC-Co - I. Effect of the C/W ratio on the morphology and defects of the WC grains*, Phys. Stat. Sol. A **193**, 271 (2002).
- [37] K. Mannesson, M. Elfving, A. Kusoffsky, S. Norgren, and J. Ågren, *Analysis of WC grain growth during sintering using electron backscatter diffraction and image analysis*, Int. J. Refract. Met. Hard Mater. **26**, 449 (2008).
- [38] A. P. Sutton and R. W. Balluffi, *Interfaces in Crystalline Materials* (Oxford University Press, Oxford, 1996).

- [39] S. Hagège, G. Nouet, and P. Delavignette, *Grain boundary analysis in TEM - IV. Coincidence and the associated defect structure in tungsten carbide*, Phys. Stat. Sol. A **61**, 97 (1980).
- [40] F. J. Humphreys, *Review - grain and subgrain characterisation by electron backscatter diffraction*, J. Mater. Sci. **36**, 3833 (2001).
- [41] C.-S. Kim and G. S. Rohrer, *Geometric and crystallographic characterization of WC surfaces and grain boundaries in WC-Co composites*, Interface Sci. **12**, 19 (2004).
- [42] J.-D. Kim, S.-J. Kang, and J.-W. Lee, *Formation of grain boundaries in liquid-phase-sintered WC-Co alloys*, J. Am. Ceram. Soc. **88**, 500 (2005).
- [43] V. Kumar, Z. Z. Fang, S. I. Wright, and M. M. Nowell, *An analysis of grain boundaries and grain growth in cemented tungsten carbide using orientation imaging microscopy*, Metall. Mater. Trans. A **37**, 599 (2006).
- [44] C.-S. Kim, T. R. Massa, and G. S. Rohrer, *Interface character distributions in WC-Co composites*, J. Am. Ceram. Soc. **91**, 996 (2008).
- [45] J. Weidow, J. Zackrisson, B. Jansson, and H.-O. Andrén, *Characterisation of WC-Co with cubic carbide additions*, Int. J. Refract. Met. Hard Mater. **27**, 244 (2009).
- [46] S. Lay and M. Loubradou, *Characteristics and origin of clusters in submicron wc-co cermets*, Philos. Mag. **83**, 2669 (2003).
- [47] M. Christensen and G. Wahnström, *Co-phase penetration of WC(10 $\bar{1}$ 0)/WC(10 $\bar{1}$ 0) grain boundaries from first principles*, Phys. Rev. B **67**, 115415 (2003).
- [48] N. K. Sharma, I. D. Ward, H. L. Fraser, and W. S. Williams, *STEM analysis of grain boundaries in cemented carbides*, J. Am. Ceram. Soc. **63**, 194 (1980).
- [49] A. Henjered, M. Hellsing, H.-O. Andrén, and H. Nordén, *Quantitative microanalysis of carbide/carbide interfaces in WC-Co-base cemented carbides*, Mater. Sci. Technol. **2**, 847 (1986).
- [50] J. Vicens, M. Benjdir, G. Nouet, A. Dubon, and J. Y. Laval, *Cobalt intergranular segregation in WC-Co composites*, J. Mater. Sci. **29**, 987 (1994).
- [51] M. Christensen and G. Wahnström, *Effects of cobalt intergranular segregation on interface energetics in WC-Co*, Acta Mater. **52**, 2199 (2004).
- [52] V. Bounhoure, S. Lay, M. Loubradou, and J. M. Missiaen, *Special WC/Co orientation relationships at basal facets of WC grains in WC-Co alloys*, J. Mater. Sci. **43**, 892 (2008).

- [53] K. Mohan and P. R. Strutt, *Observation of Co nanoparticle dispersions in WC nanograins in WC-Co cermet consolidated from chemically synthesized powders*, *Nanostruct. Mater.* **7**, 547 (1996).
- [54] K. Mohan and P. R. Strutt, *Microstructure of spray converted nanostructured tungsten carbide-cobalt composite*, *Mater. Sci. Eng., A* **209**, 237 (1996).
- [55] V. Bounhoure, J. M. Missiaen, S. Lay, and E. Pauty, *Discussion of nonconventional effects in solid-state sintering of cemented carbides*, *J. Am. Ceram. Soc.* **92**, 1396 (2009).
- [56] G. Östberg, K. Buss, M. Christensen, S. Norgren, H.-O. Andrén, D. Mari, G. Wahnström, and I. Reineck, *Effect of TaC on plastic deformation of WC-Co and Ti(C,N)-WC-Co*, *Int. J. Refract. Met. Hard Mater.* **24**, 145 (2006).
- [57] K. Hayashi, Y. Fuke, and H. Suzuki, *Effects of addition carbides on the grain size of WC-Co alloy*, *J. Jpn. Inst. Powder Powder Metall.* **19**, 67 (1972).
- [58] R. M. German, *Sintering theory and practice* (John Wiley and Sons, Inc., New York, 1996).
- [59] X. Wang, Z. Z. Fang, and H. Y. Sohn, *Grain growth during the early stage of sintering of nanosized WC-Co powder*, *Int. J. Refract. Met. Hard Mater.* **26**, 232 (2008).
- [60] G. W. Greenwood, *The growth of dispersed precipitates in solutions*, *Acta Metall.* **4**, 243 (1956).
- [61] R. Warren and M. B. Waldron, *Microstructural development during the liquid-phase sintering of cemented carbides*, *Powder Metall.* **15**, 166 (1972).
- [62] Y. J. Park, N. M. Hwang, and D. Y. Yoon, *Abnormal growth of faceted (WC) grains in a (Co) liquid matrix*, *Metall. Mater. Trans. A* **27**, 2809 (1996).
- [63] S. D. Peteves and R. Abbaschian, *Growth kinetics of solid-liquid Ga interfaces: Part II. theoretical*, *Metall. Trans. A* **22**, 1271 (1991).
- [64] G. S. Rohrer, C. L. Rohrer, and W. W. Mullins, *Coarsening of faceted crystals*, *J. Am. Ceram. Soc.* **85**, 675 (2002).
- [65] M. K. Kang, D.-Y. Kim, and N. M. Hwang, *Ostwald ripening kinetics of angular grains dispersed in a liquid phase by two-dimensional nucleation and abnormal grain growth*, *J. Eur. Ceram. Soc.* **22**, 603 (2002).
- [66] J. Kishino, H. Nomura, S.-G. Shin, H. Matsubara, and T. Tanase, *Computational study on grain growth in cemented carbides*, *Int. J. Refract. Met. Hard Mater.* **20**, 31 (2002).

- [67] O. Lavergne and C. H. Allibert, *Dissolution mechanism of tungsten carbide in cobalt-based liquids*, High Temp.-High Press. **31**, 347 (1999).
- [68] A. Jaroenworarluck, T. Yamamoto, Y. Ikuhara, T. Sakuma, T. Taniuchi, K. Okada, and T. Tanase, *Segregation of vanadium at the WC/Co interface in VC-doped WC-Co*, J. Mater. Res. **13**, 2450 (1998).
- [69] T. Yamamoto, Y. Ikuhara, and T. Sakuma, *High resolution transmission electron microscopy study in VC-doped WC-Co compound*, Sci. Technol. Adv. Mater. **1**, 97 (2000).
- [70] S. Lay, S. Hamar-Thibault, and A. Lackner, *Location of VC in VC, Cr<sub>3</sub>C<sub>2</sub> codoped WC-Co cermets by HREM and EELS*, Int. J. Refract. Met. Hard Mater. **20**, 61 (2002).
- [71] S. Lay, J. Thibault, and S. Hamar-Thibault, *Structure and role of the interfacial layers in VC-rich WC-Co cermets*, Philos. Mag. **83**, 1175 (2003).
- [72] M. Kawakami, O. Terada, and K. Hayashi, *Effect of sintering cooling rate on V segregation amount at WC/Co interface in VC-doped WC-Co fine-grained hardmetal*, J. Jpn. Soc. Powder Powder Metall. **51**, 576 (2004).
- [73] D. N. Seidman and K. Stiller, *An atom-probe tomography primer*, MRS Bull. **34**, 717 (2009).
- [74] M. Kawakami, O. Terada, and K. Hayashi, in *Proceedings of the 16th International Plansee Seminar, vol. 2*, edited by G. Kneringer, P. Rödhammer, and H. Wildner (Plansee Holding AG, Reutte, Tyrol, Austria, 2005), p. 653.
- [75] M. Kawakami, O. Terada, and K. Hayashi, *HRTEM microstructure and segregation amount of dopants at WC/Co interfaces in TiC and TaC mono-doped WC-Co submicro-grained hardmetals*, J. Jpn. Soc. Powder Powder Metall. **53**, 166 (2006).
- [76] T. Yamamoto, Y. Yamanaka, T. Taniuchi, F. Shirase, T. Tanase, and Y. Ikuhara, in *Proceedings of the 17th International Plansee Seminar, vol. 3*, edited by L. S. Sigl, P. Rödhammer, and H. Wildner (Plansee Group, Reutte, Tyrol, Austria, 2009), p. AT5.
- [77] Y. Yamanaka, T. Taniuchi, F. Shirase, T. Tanase, Y. Ikuhara, and T. Yamamoto, *High resolution electron microscopy study in ZrC-doped WC-12mass%Co alloys*, Mater. Trans., JIM **50**, 1096 (2009).
- [78] A. Delanoë, M. Bacia, E. Pauty, S. Lay, and C. H. Allibert, *Cr-rich layer at the WC/Co interface in Cr-doped WC-Co cermets: segregation or metastable carbide?*, J. Cryst. Growth **270**, 219 (2004).

- [79] S. Lay, M. Loubradou, and W.-D. Schubert, *Structural analysis on planar defects formed in WC platelets in Ti-doped WC-Co*, J. Am. Ceram. Soc. **89**, 3229 (2006).
- [80] B. Wittmann, W.-D. Schubert, and B. Lux, *WC grain growth and grain growth inhibition in nickel and iron binder hardmetals*, Int. J. Refract. Met. Hard Mater. **20**, 51 (2002).
- [81] R. W. K. Honeycombe and H. K. D. H. Bhadeshia, *Steels - Microstructure and Properties*, 2nd ed. (Butterworth-Heinemann, Oxford, 1995).
- [82] J. P. Hirth and J. Lothe, *Theory of Dislocations*, 2nd ed. (Wiley, New York, 1982).
- [83] T. C. Bor, A. T. W. Kempen, F. D. Tichelaar, E. J. Mittemeijer, and E. van der Geissen, *Diffraction-contrast analysis of misfit strains around inclusions in a matrix: VN particles in  $\alpha$ -Fe*, Philos. Mag. A **82**, 971 (2002).
- [84] N. W. Ashcroft and N. D. Mermin, *Solid State Physics* (Brooks/Cole, United States, 1976).
- [85] R. M. Martin, *Electronic Structure - Basic Theory and Practical Methods* (Cambridge University Press, Cambridge, 2004).
- [86] P. Hohenberg and W. Kohn, *Inhomogeneous electron gas*, Phys. Rev. **136**, B864 (1964).
- [87] M. Levy, *Universal variational functionals of electron densities, first-order density matrices, and natural spin-orbitals and solution of the  $v$ -representability problem*, Proc. Natl. Acad. Sci. USA **76**, 6062 (1979).
- [88] W. Kohn and L. J. Sham, *Self-consistent equations including exchange and correlation effects*, Phys. Rev. **140**, A1133 (1965).
- [89] O. Gunnarsson and B. I. Lundqvist, *Exchange and correlation in atoms, molecules, and solids by the spin-density-functional formalism*, Phys. Rev. B **13**, 4274 (1976).
- [90] D. M. Ceperley and B. J. Alder, *Ground state of the electron gas by a stochastic method*, Phys. Rev. Lett. **45**, 566 (1980).
- [91] J. P. Perdew, J. A. Chevary, S. H. Vosko, K. A. Jackson, M. R. Pederson, D. J. Singh, and C. Fiolhais, *Atoms, molecules, solids, and surfaces: Applications of the generalized gradient approximation for exchange and correlation*, Phys. Rev. B **46**, 6671 (1992).
- [92] J. P. Perdew, K. Burke, and M. Ernzerhof, *Generalized gradient approximation made simple*, Phys. Rev. Lett. **77**, 3865 (1996).

- [93] A. E. Mattsson, R. Armiento, P. A. Schultz, and T. R. Mattsson, *Nonequivalence of the generalized gradient approximations PBE and PW91*, Phys. Rev. B **73**, 195123 (2006).
- [94] J. P. Perdew, A. Ruzsinszky, G. I. Csonka, O. A. Vydrov, G. E. Scuseria, L. A. Constantin, X. Zhou, and K. Burke, *Restoring the density-gradient expansion for exchange in solids and surfaces*, Phys. Rev. Lett. **100**, 136406 (2008).
- [95] M. Ropo, K. Kokko, and L. Vitos, *Assessing the Perdew-Burke-Ernzerhof exchange-correlation density functional revised for metallic bulk and surface systems*, Phys. Rev. B **77**, 195445 (2008).
- [96] H. J. Monkhorst and J. D. Pack, *Special points for Brillouin-zone integrations*, Phys. Rev. B **13**, 5188 (1976).
- [97] M. Methfessel and A. T. Paxton, *High-precision sampling for Brillouin-zone integration in metals*, Phys. Rev. B **40**, 3616 (1989).
- [98] P. E. Blöchl, *Projector augmented-wave method*, Phys. Rev. B **50**, 17953 (1994).
- [99] G. Kresse and J. Joubert, *From ultrasoft pseudopotentials to the projector augmented wave method*, Phys. Rev. B **59**, 1758 (1999).
- [100] M. W. Finnis and J. E. Sinclair, *A simple empirical n-body potential for transition metals*, Philos. Mag. A **50**, 45 (1984).
- [101] J. K. Nørskov and N. D. Lang, *Effective-medium theory of chemical binding: Application to chemisorption*, Phys. Rev. B **21**, 2131 (1980).
- [102] M. S. Daw and M. I. Baskes, *Semiempirical, quantum mechanical calculation of hydrogen embrittlement in metals*, Phys. Rev. Lett. **50**, 1285 (1983).
- [103] G. Simonelli, R. Pasianot, and E. J. Savino, *Embedded-atom-method interatomic potentials for bcc-iron*, Mat. Res. Soc. Symp. Proc. **291**, 567 (1993).
- [104] J. H. Rose, J. R. Smith, F. Guinea, and J. Ferrante, *Universal features of the equation of state of metals*, Phys. Rev. B **29**, 2963 (1984).
- [105] D. J. Bacon, D. M. Barnett, and R. O. Scattergood, *Anisotropic continuum theory of lattice defects*, Prog. Mat. Sci. **23**, 51 (1980).
- [106] J. O. Kim and J. D. Achenbach, *Elastic constants of single-crystal transition-metal nitride films measured by line-focus acoustic microscopy*, J. Appl. Phys. **72**, 1805 (1992).
- [107] J. D. Eshelby, W. T. Read, and W. Shockley, *Anisotropic elasticity with applications to dislocation theory*, Acta Metall. **1**, 251 (1953).

- [108] A. N. Stroh, *Dislocations and cracks in anisotropic elasticity*, Philos. Mag. **3**, 625 (1958).
- [109] K. Malén and J. Lothe, *Explicit expressions for dislocation derivatives*, Phys. Status Solidi **39**, 287 (1970).
- [110] D. M. Barnett and J. Lothe, *Synthesis of the sextic and the integral formalism for dislocations, greens function and surface waves in anisotropic elastic solids*, Phys. Norv. **7**, 13 (1973).
- [111] D. M. Barnett and J. Lothe, *Line force loadings on anisotropic half-spaces and wedges*, Phys. Norv. **8**, 13 (1975).
- [112] D. M. Barnett and J. Lothe, *An image force theorem for dislocations in anisotropic bicrystals*, J. Phys.: Metal Phys. **4**, 1618 (1974).
- [113] M. W. Finnis, *The theory of metal-ceramic interfaces*, J. Phys.: Condens. Matter **8**, 5811 (1996).
- [114] L. Ramqvist, *Wetting of metallic carbides by liquid copper, nickel, cobalt and iron*, Int. J. Powder Metall. **1**, 2 (1965).
- [115] J. P. Hirth and J. R. Rice, *On the thermodynamics of adsorption at interfaces as it influences decohesion*, Metall. Trans. A **11**, 1501 (1980).
- [116] R. Warren, *Determination of the interfacial energy ratio in two-phase systems by measurement of interphase contact*, Metallography **9**, 183 (1976).
- [117] R. Warren, *Solid-liquid interfacial energies in binary and pseudo-binary systems*, J. Mater. Sci. **15**, 2489 (1980).
- [118] X.-G. Wang, A. Chaka, and M. Scheffler, *Effect of the environment on  $\alpha$ - $Al_2O_3$  (0001) surfaces*, Phys. Rev. Lett. **84**, 3650 (2000).
- [119] K. Reuter and M. Scheffler, *Composition, structure, and stability of  $RuO_2(110)$  as function of oxygen pressure*, Phys. Rev. B **65**, 035406 (2001).
- [120] W. Zhang, J. R. Smith, and X.-G. Wang, *Thermodynamics from ab initio computations*, Phys. Rev. B **70**, 024103 (2004).
- [121] P. Gustafson, *An evaluation of the thermodynamic properties and the P,T phase diagram of carbon*, Carbon **24**, 169 (1986).
- [122] D. A. Andersson, P. A. Korzhavyi, and B. Johansson, *First-principles based calculation of binary and multicomponent phase diagrams for titanium carbonitride*, CALPHAD **32**, 543 (2008).
- [123] E. Ziambaras, J. Kleis, E. Schröder, and P. Hyldgaard, *Potassium intercalation in graphite: A van der Waals density-functional study*, Phys. Rev. B **76**, 155425 (2007).

- [124] G.-X. Qian, R. M. Martin, and D. J. Chadi, *First-principles study of the atomic reconstructions and energies of Ga- and As-stabilized GaAs(100) surfaces*, Phys. Rev. B **38**, 7649 (1988).
- [125] P. Gustafson, *Evaluation of the thermodynamic properties of tungsten*, Int. J. Thermophys. **6**, 395 (1985).
- [126] S. Jonsson, *Phase relations in quaternary hard materials*, Ph.D. thesis, The Royal Institute of Technology, Stockholm, 1993.
- [127] K. Reuter and M. Scheffler, *Erratum: Composition, structure, and stability of RuO<sub>2</sub>(110) as function of oxygen pressure*, Phys. Rev. B **75**, 049901(E) (2007).
- [128] E. I. Isaev, S. I. Simak, I. A. Abrikosov, R. Ahuja, Y. K. Vekilov, M. I. Katsnelson, A. I. Lichtenstein, and B. Johansson, *Phonon related properties of transition metals, their carbides, and nitrides: A first-principles study*, J. Appl. Phys. **101**, 123519 (2007).
- [129] S. Baroni, S. de Gironcoli, A. D. Corso, and P. Gianozzi, *Phonons and related crystal properties from density-functional perturbation theory*, Rev. Mod. Phys. **73**, 515 (2001).
- [130] D. R. Gaskell, in *Physical metallurgy*, edited by R. W. Cahn and P. Haasen (Elsevier Science, Amsterdam, the Netherlands, 1996).
- [131] A. V. Ruban and I. A. Abrikosov, *Configurational thermodynamics of alloys from first principles: effective cluster interactions*, Rep. Prog. Phys. **71**, 046501 (2008).
- [132] M. Christensen, G. Wahnström, S. Lay, and C. H. Allibert, *Morphology of WC grains in WC-Co alloys: Theoretical determination of grain shape*, Acta Mater. **55**, 1515 (2007).
- [133] R. E. Peierls, *The size of a dislocation*, Proc. Phys. Soc. **52**, 34 (1940).
- [134] F. R. N. Nabarro, *Dislocations in a simple cubic lattice*, Proc. Phys. Soc. **59**, 256 (1947).
- [135] J. Q. Broughton and G. H. Gilmer, *Molecular dynamics investigation of the crystal-fluid interface. VI. Excess surface free energies of crystal-liquid systems*, J. Chem. Phys. **84**, 5759 (1986).
- [136] M. Guttman, *Equilibrium segregation in a ternary solution: A model for temper embrittlement*, Surf. Sci. **53**, 213 (1975).
- [137] P. Lejček and S. Hofmann, *Thermodynamics of grain boundary segregation and applications to anisotropy, compensation effect and prediction*, Crit. Rev. Solid State Mater. Sci. **33**, 133 (2008).

- [138] J. Weidow and H.-O. Andrén, *Grain and phase boundary segregation in WC-Co with small V, Cr or Mn additions*, accepted for publication in Acta Mater.



# Paper I

## **Theory of ultrathin films at metal-ceramic interfaces**

S. A. E. Johansson and G. Wahnström

Accepted for publication in Phil. Mag. Lett.



# Paper II

**A computational study of cubic carbide films in WC/Co interfaces**

S. A. E. Johansson and G. Wahnström

In manuscript.



## Paper III

### **Energetics and structure of interfaces in WC-Co alloys from first-principles calculations**

M. Slabanja, S. A. E. Johansson and G. Wahnström

In: L. S. Sigl, P. Rödhammer, H. Wildner (Eds.), Proceedings of the 17th International Plansee Seminar, vol. 2, Plansee Group, Reutte, Tyrol, Austria, 2009, p. HM2.



# Paper IV

## **Transition metal solubilities in WC in cemented carbide materials**

J. Weidow, S. A. E. Johansson, H.-O. Andrén and G. Wahnström

Submitted to J. Am. Ceram. Soc.



# Paper V

## **Interface energy of semicoherent metal-ceramic interfaces**

S. A. E. Johansson, M. Christensen and G. Wahnström

Phys. Rev. Lett. **95**, 226108 (2005).



# Paper VI

**Theoretical investigation of moderate misfit and interface energetics in the Fe/VN system**

D. H. R. Fors, S. A. E. Johansson, M. Petisme and G. Wahnström

In manuscript.

